Int J Fract
https://doi.org/10.1007/s10704-024-00813-3

RESEARCH

Wave interactions and fracture evolution in a thin glass plate under impact: a combined experimental and peridynamic analysis

Yenan Wang · Chian-Fong Yen · Jian Yu · Jared Wright · Florin Bobaru

Received: 18 August 2023 / Accepted: 12 August 2024

Abstract We perform experiments and peridynamic simulations to understand the evolution of cracks in a thin glass plate, backed by a polycarbonate plate, impacted by a small projectile at 150 m/s. We use the peridynamic model to investigate how various types of crack systems are generated by the impact event and how they evolve in time. The detailed investigations of wave interactions and the different cracks and failure types they generate, performed using the peridynamic model, are unique. Post-mortem analysis of glass fragments allows comparisons with the computational results in terms of the kind and location of crack systems. Fractography results provide information about the growth direction for some of the edge cracks and the peridynamic results are used to explain the particular wave interactions leading to the observed behavior. The model captures, in an average sense, some wispy/very fine cracks (surface roughness) experimentally observed on fragments coming from the ends of the Hertzian-cone crack. This is the first attempt at using a computational model to predict the fine details and complex mechanisms of the origin and time evolution of fracture and full fragmentation in a glass plate from impact.

Keywords Peridynamics · Dynamic fracture · Stress waves · Glass · Fractography · Hertz cone crack · Impact · Lamb waves

Supplementary Information The online version contains supplementary material available at https://doi.org/10.1007/s10704-024-00813-3.

Y. Wang · F. Bobaru (✉)
Mechanical and Materials Engineering, University of Nebraska-Lincoln, Lincoln, NE, USA
e-mail: fbobaru2@unl.edu

Y. Wang
Tianjin University of Science and Technology, Tianjin, China

C.-F. Yen · J. Yu · J. Wright
Army Research Laboratory, Aberdeen Proving Ground, Aberdeen, MD, USA

J. Wright
Work Performed Under Bowhead S&T. Currently at NAVAIR, Patuxent River, MD, USA

1 Introduction

Dynamic brittle crack growth, as the initiation of material failure, remains a challenging problem after more than a century of research (Walley 2014, Zhang et al. 2015). The interaction between stress waves and propagating cracks is difficult to simulate because such interactions often lead to a variety of failure types, including diffuse damage, localized cracks, and fragmentation. Capturing all of this complex behavior with a computational model is not a simple task (Song et al. 2008; Marder 2015; Bobaru and Zhang 2015; Pyttel et al. 2011; Timmel et al. 2007; Seagraves and

Published online: 05 December 2024

Radovitzky 2015). In the present work, we provide a detailed analysis, based on a peridynamic model, of the evolution of failure and damage in a thin glass plate impacted by a small projectile. For this purpose, we use a simple peridynamic model with a linear-elastic and brittle micro-scale constitutive relation (see Hu et al. 2013; Bobaru et al. 2012) to simulate the experimentally observed fracture and damage produced by impact on a 10 cm × 10 cm × 3.3 mm glass plate with a polycarbonate backing plate of similar dimensions. We show that a peridynamic approach that *uses a minimal set of input parameters* is able to reproduce the large variety of failure modes generated when a thin glass plate is hit by a small projectile at a speed of 150 m/s: circumferential cracks, radial cracks and cracks parallel with the sides of the plate, fragmentation and formation of glass chips, and edge-to-center cracks. We analyze the computational results in relation to experimental ones in terms of the damage and failure patterns, the growth direction for edge-cracks, and some fine features/roughness observed on certain crack surfaces. Our computations show that this type of roughness happens, surprisingly, at low crack propagation speeds. We conduct fractography experiments to understand the direction of crack growth of some edge-cracks. The peridynamic simulations provide evidence that demonstrate/illustrate the underlining failure mechanisms of various types of cracks. In such brittle systems, wave interactions/reinforcement is the major contributor to crack formation and propagation. Our analysis identifies which wave reinforcements are responsible for which types of cracks. In a previous paper (Hu et al. 2013), we only compared the experimental results with the peridynamic simulations in terms of the overall damage patterns under different impact velocities.

We assume that the material response of glass, for the impact speed analyzed here, is essentially brittle, with negligible plastic/viscous dissipation. Besides glass, many other material systems, like inorganic glasses, ceramic materials, concrete, and certain metals or metallic alloys, do behave in a brittle way when loaded dynamically, as is the case for projectile impact or plate impact (Knight et al. 1977; Sherman 2000; Sherman and Tamir 1988).

The question of how damage progresses in time and how brittle materials fail when impacted by a projectile is important when trying to improve design of materials and structures. For instance, understanding of how the thin glass of a smart-phone cracks when it impacts a hard object, and why, by simply adding a thin scratch-protective membrane on top leads to improved crack resistance, depends on understanding the complex dynamics of crack growth in a brittle plate from impact.

From a qualitative point of view, brittle damage is characterized by a large number of cracks and fragments that strongly interact with one another and with stress waves. These types of problems have been difficult to computationally model/simulate in the past, and, to the best of our knowledge, no computational model can accurately describe the entire evolution of brittle damage, from the initiation stages to the post-fracture and fragmentation phase. More often than not, to even obtain some partial solutions to the problem of brittle damage from impact, *one has to "insert" parts of the solution into the model*, by ways of, for example, criteria for failure, preferred directions for crack growth, etc. This approach may work for cases like crack initiation and propagation of a single crack, but they are unlikely to work well when the fracture process leads to complex multi-crack interactions and fragmentation.

Most prior computational works discussing the failure of brittle materials (like glass or glassy polymers) from impact resorted to using the Finite Element Method (FEM), alone or in combination with the Discrete Element Method (Pyttel et al. 2011; Timmel et al. 2007; Rudshaug et al. 2023; Lei et al. 2021; Chen and Chan 2018; Hirobe et al. 2023). These approaches employ element-deletion, cohesive-zone, or other types of damage models to simulate the evolution of impact-induced fracture and fragmentation in brittle targets. While Phase-Field models have also been introduced to model brittle fracture (Borden et al. 2012), they appear to have not been used for impact-fragmentation types of phenomena. The Discontinuous-Galerkin method has also been used for simulating impact on brittle targets. In reference (Seagraves and Radovitzky 2015), for example, the authors develop a Discontinuous Galerkin method for a strain-dependent elasto-plastic model in which fracture is simulated via a Cohesive Zone model that is also assumed to be strain-rate dependent. The model is used to simulate impact damage on brittle targets. Edge-on impact and normal impact simulations in alumina are shown. For normal impact on a thin plate,

the model is able to capture Hertz cone crack formation, growth of radial cracks and circumferential cracks. While perhaps one of the most successful type of simulations of impact damage on brittle plates to date, this model does not match experimentally measured crack propagation speeds in the edge-on impact case. For the normal impact, the authors of Seagraves and Radovitzky (2015) mostly discuss the damage patterns and the dependence of these patterns on the impact velocity, similar to what is done in the peridynamics-based papers (Hu et al. 2013) and (Bobaru et al. 2012) for glass. Some discussion on the possible reasons behind the growth of the various types of cracks is presented in Seagraves and Radovitzky (2015), but the actual mechanisms/scenarios behind such phenomena are not identified.

The goal of our paper is to uncover, using the peridynamic model, the interactions that lead to the formation of each crack system in the failure of the glass plate under normal impact. The results we obtain here rely on a simple, basic damage mechanism and simple linear-elastic with brittle failure constitutive law at the micro-scale. The fact that such a simple model can encompass modeling the large variety of failure modes (from radial and circumferential cracks, to fragmentation, and anything in-between) observed in the impact-induced fracture and fragmentation of a thin glass plate, tells us that other ingredients (like plasticity, strain-rate dependency other than inertia-induced ones, etc.) have a *second-order influence* on the damage and failure behavior of glass plates, at least at the impact speeds tested here (up to several hundreds of meters per second). We will also show that what appears to be branching cracks near the edges of the plate are in fact the meeting of two different types of cracks, not the splitting of a single crack into two cracks. The model finds that roughness on the glass chips at the ends of the Hertz-cone crack are, surprisingly, produced at very low crack propagation speeds. We discover that the bouncing of a train of shear waves through the thickness of the plate are responsible for the critical hoop strain required to sustain/maintain the growth of radial cracks at speeds lower than the surface wave speeds but higher than the "support" value given by the in-plane propagation speed of these through-thickness reflected waves. We also see that edge-to-center cracks are induced by the "folding" of the shear wave, as it reflects from the sides of the plate and reinforces incident surface waves. We provide partial experimental validation for this point. Cracks that develop parallel to the plate's sides are shown to be caused by the reinforcement between the incident shear or Rayleigh waves with the (direct or through-thickness bouncing) shear component of the longitudinal incident wave reflected from the sides of the plate. While for most of the computational results we provide direct or indirect experimental evidence, some aspects on which the simulations shine light on still require experimental validation, and we are eager to learn of future experiments that might be able to do that.

The paper is organized as follows: Sect. 2 describes the experimental setup and parameters used in the computational model that discretizes the peridynamic formulation; Sect. 3 gives an brief overview of the PD model and discretization used; Convergence tests are shown in Appendix A; The evolution of fracture and damage, and comparisons with experiments are presented in Sect. 4, in which, after a general overview of the main events, we focus attention to the different crack systems: ring cracks, Hertzian-cone crack, wispy ridges on some crack surfaces, radial cracks, cracks parallel to the sides of the plate, and boundary cracks (edge-to-center cracks). For each of these crack systems obtained by peridynamic simulations, we compare their configuration and location with our experimental observations, and we monitor, computationally, their propagation speed. Whenever possible (as in the case of ring cracks), we compare against analytical and experimental solutions available in the published literature. We present final summary and conclusions in Sect. 5.

2 Experimental and computational model setup

We consider the following material system (see Figs. 1 and 2): a thin plate glass, of dimensions $10.16 \times 10.16 \times 0.33$ cm, and a backing plate of polycarbonate (PC) of dimensions $10.16 \times 10.16 \times 0.3$ cm, impacted by a small steel projectile at a speed of 150 m/s. A study on the variation of damage with impact speed has been published in Hu et al. (2013). The glass plate serves as

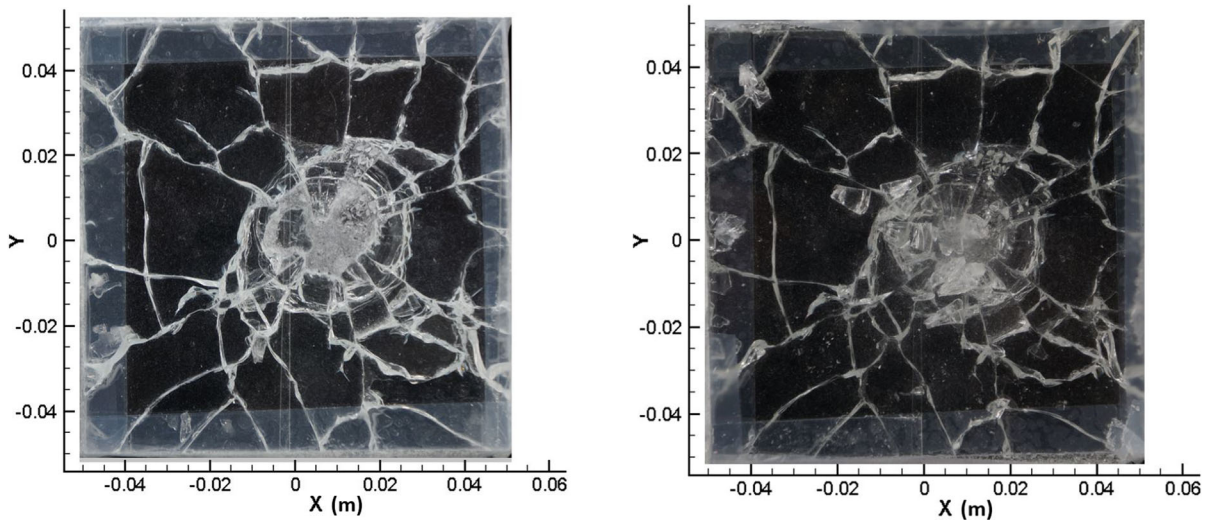

Fig. 1 Photos of the post-mortem sample from experiment. View from the strike (left) and back face (right) of the glass plate. All geometrical dimensions shown in this paper are in meters, unless otherwise specified

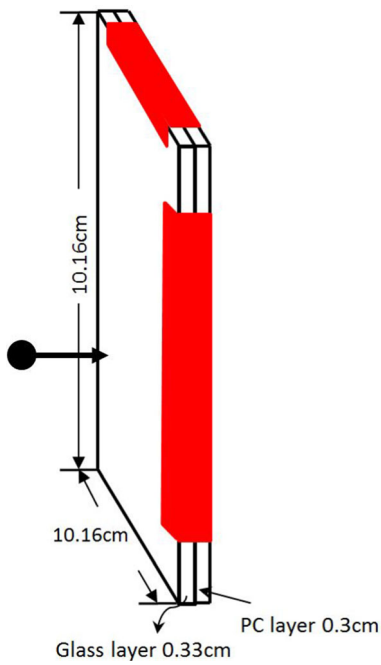

Fig. 2 Schematic of the experimental setup for the impact on the two-plate system. Scotch tape was used only on the sides, to hold the plates together

a model of brittle fracture and its dimensions will allow us to understand both the bulk material behavior as well as the connection material-structure and its influence on the evolution of damage in brittle fracture.

With the goal of understanding how cracks form and grow from impact on a thin glass plate, we chose to use the backing plate in order to preserve glass fragments for post-mortem analysis. The two plates are taped together along their sides *only*. Post-mortem we applied tape on the front face of the sample to avoid movement of fragments. To avoid complex stress-waves interactions with boundaries, which in brittle fracture have a significant influence on the results (see Hu et al. 2013; Bobaru et al. 2012), the two plates are freely suspended by tape. A small steel projectile (sphere of 440C stainless steel with a diameter of 0.556 cm and mass of 0.692 g) impacts the glass surface at 150 m/s. The impact location is slightly off-center (about 0.8 mm below the horizontal symmetry axis, and 9.7 mm closer to the right edge. This off-center impact happened by chance in the experiments. We used the same impact location in the peridynamic simulations. As we shall see, having an off-center impact is extremely useful in determining and explaining the cause of initiation, growth and propagation of various crack systems that are generated by the impact event.

The material properties of the soda-lime glass used in the experiment are: Young's modulus $E^{\text{glass}} = 72$ GPa, shear modulus $\mu^{\text{glass}} = 30$ GPa (thus the bulk modulus is $\kappa^{\text{glass}} = 43$ GPa and the Poisson ratio is $\upsilon^{\text{glass}} = 0.22$). These parameters give a longitudinal wave speed of $C_1^{\text{glass}} = 5432$ m/s, a shear wave speed

$C_2^{\text{glass}} = 3506$ m/s, and the surface wave speed of $C_R^{\text{glass}} = 3139$ m/s. We note that variations of ten percent in material properties of soda lime glass are not unusual. For instance, the Poisson ratio value given in Bowden and Field (1964) is 0.24.

The material properties for the polycarbonate backing plate, which does not suffer any damage at the impact speed used in our study, are: $E^{\text{PC}} = 2$ GPa, shear modulus $\mu^{\text{PC}} = 0.73$ GPa (thus the bulk modulus is $\kappa^{\text{PC}} = 2.56$ GPa and Poisson ratio $\nu^{\text{PC}} = 0.37$). These parameters give a longitudinal wave speed of $C_1^{\text{PC}} = 1960$ m/s, a shear wave speed $C_2^{\text{PC}} = 1131$ m/s, and the surface wave speed of $C_R^{\text{PC}} = 1029$ m/s. The surface wave speed is calculated from the following equation (Rahman and Michelitsch 2006):

$$\mathrm{R(V)} = (2 - M_2^2)^2 - 4\sqrt{(1 - M_1^2)(1 - M_2^2)} = 0 \tag{1}$$

Here, $M_1 = V/c_1$, $M_2 = V/c_2$, and $c_1 = \sqrt{(\lambda + 2\mu)/\rho}$, $c_2 = \sqrt{\mu/\rho}$ are dilatational and shear wave speeds, respectively.

The computational model uses the same geometry and conditions as in the experiments, with one difference in the boundary conditions: we do not implement conditions that would mimic the tape on the sides of the plates. While the response will be, therefore, different between the experiments and the simulations, these differences are not going to qualitatively modify the conclusions we draw. We notice that, for example, even if we conduct simulations with the glass plate only (no backing PC plate), we observe (see Movie 1) that qualitatively the resulting damage patterns are similar, roughly, to those from the experiment, which includes tape on the sides, and the PC backing plate. The tape in the experimental tests will play some role in transferring energy between the two plates and we will point out where this energy transfer likely leads to quantitative changes compared with a case in which there is no tape on the sides between the glass and the PC plates.

3 The Peridynamic model for brittle failure

The peridynamics formulation was introduced by Silling (2000). The peridynamic equations of motion are:

$$\rho\ddot{\boldsymbol{u}}(x,t) = \int_{H_x} \boldsymbol{f}(\boldsymbol{u}(\widehat{\boldsymbol{x}},t) - \boldsymbol{u}(\boldsymbol{x},t), \widehat{\boldsymbol{x}} - \boldsymbol{x}) d\boldsymbol{V}_{\widehat{\boldsymbol{x}}} + \boldsymbol{b}(\boldsymbol{x},t) \tag{2}$$

where $\boldsymbol{u}$ is the displacement vector field, $\boldsymbol{b}$ is the body force, and $\boldsymbol{f}$ is the pairwise force function in the peridynamic bond that connects material points $\widehat{\boldsymbol{x}}$ and $\boldsymbol{x}$. The integral is defined over a region $\boldsymbol{H_x}$ around point $\boldsymbol{x}$, called the "horizon region" (see Fig. 3).

For a microelastic material (Silling 2000), the force in a peridynamic bond $(\boldsymbol{x}, \widehat{\boldsymbol{x}})$ is derived from a micropotential:

$$\boldsymbol{f}(\boldsymbol{\eta}, \boldsymbol{\xi}) = \frac{\partial \omega(\boldsymbol{\eta}, \boldsymbol{\xi})}{\partial \boldsymbol{\eta}} \tag{3}$$

where $\boldsymbol{\xi} = \widehat{\boldsymbol{x}} - \boldsymbol{x}$ is the relative position vector and $\boldsymbol{\eta} = \boldsymbol{u}(\widehat{\boldsymbol{x}}, t) - \boldsymbol{u}(\boldsymbol{x}, t)$ is the relative displacement vector between $\widehat{\boldsymbol{x}}$ and $\boldsymbol{x}$. A linear microelastic material is defined by a micropotential ω:

$$\omega(\boldsymbol{\eta}, \boldsymbol{\xi}) = \frac{\mathrm{c}(\boldsymbol{\xi})\mathrm{s}^2\|\boldsymbol{\xi}\|}{2} \tag{4}$$

where $\mathrm{c}(\xi)$ is the micromodulus function and

$$\mathrm{s} = \frac{\|\boldsymbol{\xi} + \boldsymbol{\eta}\| - \|\boldsymbol{\xi}\|}{\|\boldsymbol{\xi}\|} \tag{5}$$

is the bond strain or its relative elongation. For a microelastic material, the corresponding pairwise force becomes

$$\boldsymbol{f}(\xi, \boldsymbol{\eta}) = \begin{cases} \dfrac{\boldsymbol{\xi} + \boldsymbol{\eta}}{\|\boldsymbol{\xi} + \eta\|} cs, \text{if} \|\boldsymbol{\xi}\| \le \delta \\ 0, \text{if} \|\boldsymbol{\xi}\| > \delta \end{cases} \tag{6}$$

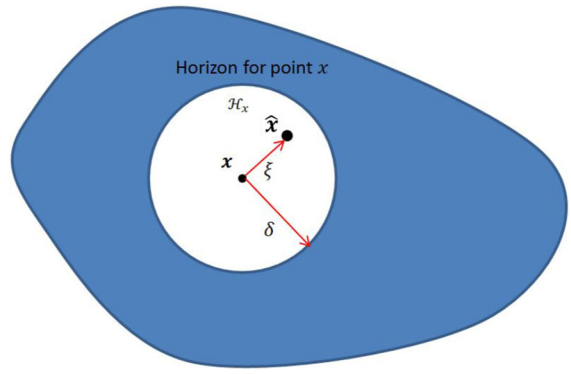

Fig. 3 The horizon region for a point $\boldsymbol{x}$ in a peridynamic model and the peridynamic bond between material points $\boldsymbol{x}$ and $\widehat{\boldsymbol{x}}$

To determine the micromodulus function, we assume a certain profile for it, e.g. constant, linearly decreasing to zero as the bond length reaches the horizon size δ, etc. (see Bobaru et al. 2009). Once a choice is made, one then computes the undetermined parameter(s) by, for example, enforcing a match between the elastic strain energy from a homogeneous deformation in a classical elastic material and the corresponding strain energy in the microelastic peridynamic material model (see Silling and Askari 2005). In this work, we use the constant micromodulus function, with its value given by:

$$c = \frac{18\kappa}{\pi\delta^4} \tag{7}$$

where κ is the the bulk modulus (note that Poisson's ratio for a bond-based model in 3D is fixed to 0.25). Other variants of the micromodulus function are possible: for example, the micromodulus function may be found so that it matches a certain material length-scale resulting from a particular microstructure (Silling 2014), while (Aguiar and Fosdick 2014) and (Aguiar 2016) propose a free energy function for an isotropic, linear elastic PD material, which depends quadratically on the infinitesimal normal and shear strain states, in analogy to the quadratic strain energy function of the classical linear theory.

When modeling homogeneous materials, the horizon size can be dictated by the size of geometrical features (notches, etc.) or by the dynamic length-scales in the problem (see Bobaru and Hu 2012). In this work, we consider the materials to be homogeneous, and we will perform δ-convergence studies (see Bobaru and Hu 2012) to determine a proper horizon size for dynamic failure in glass. In this case, the horizon size (the extent of the nonlocality in the model) can be thought of as representing the fracture process zone in glass under dynamic loading conditions. In (Bobaru and Zhang 2015), a value of $\delta \approx 1$ mm was found to result in a dynamic crack propagation speed *in glass* close to measured values. In the Appendix A we test several different values of the PD horizon and also observe that while general damage features are common between the results, those obtained with $\delta \approx 1$ mm match better the number of the larger fragments produced by the impact event. Similar ways of selecting the size of the PD horizon based on experimental measurements have been discussed in Xu et al. (2018).

To model brittle failure, we assume that there exists a critical bond strain, or relative elongation s_0, at which a bond no longer carries a load. The deformation of a micro-elastic material is history dependent (see Silling and Bobaru 2005). The parameter s_0, for bonds in the bulk, is obtained by matching the peridynamic fracture energy, required to completely separate a body into two halves across a fracture plane by breaking all the bonds that initially connected points in the opposite halves, to the material's fracture energy G_0 (see Silling and Askari 2005). In 3D, this match leads to:

$$G_0 = \int_0^{\delta}\int_0^{2\pi}\int_z^{\delta}\int_0^{cos^{-1}(z/r)} \frac{cs_0^2 r}{2} r^2 sin\phi d\phi dr d\theta dz \tag{8}$$

For the constant micromodulus in 3D (see (Ha and Bobaru 2010) for the case of "conical" micromodulus function in 2D) we have

$$s_0 = \sqrt{\frac{5G_0}{9\kappa\delta}} \tag{9}$$

This simplest elastic-brittle failure model has two limitations: crack nucleation is linked to the horizon size (horizon-dependent strength), and mixed-mode fracture is tied to mode I failure (mode II is not independent from mode I fracture). Two-parameter (or more) bond-failure models are needed to create PD models in which nucleation and crack growth are both independent of the horizon size, see for example (Niazi et al. 2021). For a discussion on a state-based PD model with mode II failure independent from mode I fracture please see (Wang et al. 2023). For our analysis of the glass impact problem, these two limitations are likely of secondary importance because the crack propagation phase is the dominant one and the specific relation between crack growth modes in the monolithic glass are not likely to significantly change the overall conclusions drawn. In certain problems, the independence between failure modes is critical, as in the case of failure at an interface in a multi-material system (PMMA layers bonded by epoxy, see Wang et al. 2023), where a state-based model needs to be employed.

All computations in this paper are performed using a slightly modified version of EMU (Silling 2005), which

implements the "meshfree" discretization of PD (Silling and Askari 2005). The main changes we have made to EMU are related to the spatial integration algorithm. The spatially discretized form of the peridynamic equation of motion (see Eq. 2) with a one-point Gaussian integration for the domain integral leads to:

$$\rho \ddot{\boldsymbol{u}}_{\boldsymbol{i}}^{\boldsymbol{n}}(x,t) = \sum_j c \frac{\boldsymbol{u}_j^n - \boldsymbol{u}_i^n}{\boldsymbol{x_j} - \boldsymbol{x_i}} V_{ij} + b_i^n \tag{10}$$

where V_{ij} is the volume of node j inside the horizon of node i. Note that other forms of the integrand can be used here (see Chen et al. 2016).

In (Hu et al. 2010) several different algorithms have been proposed and tested for approximating the exact nodal areas covered by the horizon. In the present paper we use the spatial integration called in Seleson (2014) the HHB algorithm, which adjusts the volumes for nodes that are partially covered by the horizon by a certain factor (see Hu et al. 2010; Seleson 2014). For details see also (Bobaru and Zhang 2015).

The material parameters in the bond-based peridynamic model (see Silling 2000) will not match exactly all the elastic constants of the glass and PC materials used here. In EMU (Silling 2005), the software used in the simulations presented in this paper, the calibration is realized by using the bulk modulus of glass and polycarbonate, respectively, and matching it for the particular discretization used. For the 3D bond-based model, the effective Poisson ratio is a fixed value 1/4. Because in EMU the match of the elastic properties is for the bulk modulus (matching therefore the longitudinal wave speed), the Young's modulus that is effectively used in the computational model only approximates the material's modulus. Since the Poisson ratio of glass is very close to the one modeled by bond-based PD, the approximation of Young's modulus for glass is better than that for the polycarbonate.

The peridynamic surface effect (bond properties derived for nodes in the bulk, when used for nodes near a boundary lead to slightly different elastic and failure behavior due to the incomplete horizon region) has been discussed in many works before (see Le and Bobaru 2018) and in many applications it can be ignored as long as the horizon size is sufficiently small. However, in impact problems, correcting it is essential because many cracks are produced at the edges by surface waves interactions with other waves (see, e.g., Hu et al. 2013). Initiation of cracks due to impact is also affected strongly by the surface effect. This is why, as seen in Bobaru et al. (2016), it is important to use surface correction methods for modeling of brittle failure induced by impact. The correction has to be performed on both the bond micromodulus and the critical bond strain. A review of various methods that can be used for surface correction is presented in Le and Bobaru (2018).

In this paper, we utilize the following corrections of the peridynamic surface effect (Le and Bobaru 2018) available in the EMU code (Silling 2005). In order to correct for the missing bonds in determining the critical bond strain, we choose to strengthen the material in damaged regions by allowing s_0 to depend on the amount of damage at that particular node. One could attempt an exact evaluation of the damage-dependent (variable) s_0. However, here we resort to a simpler way, namely an approximation also used in Silling and Askari (2005). This approximation is described by the following:

$$s_0 = \begin{cases} s_0 \times \min\left(\gamma, 1 + \beta \dfrac{D-\alpha}{1-D}\right), & \text{if } D > \alpha \\ s_0, & \text{otherwise} \end{cases} \tag{11}$$

where the nodal damage index D is defined, in its discrete version, as the ratio of the number of broken bonds to the number of initial bonds. We choose $\alpha = 0.35$, $\beta = 1$, and $\gamma = 2$ (Silling and Askari 2005).

In the model discussed here, bonds can only fail in tension. In many types of deformations, at a node there will be bonds in tension and in compression. In such case, it is natural to assume that the critical bond strain for the bonds in tension depends on how much compression there is in bonds connected to the same node, and to increase these values to account for the amount of compression. With such a dependency, a better agreement with experimental results can be seen for fracture/fragmentation in glass. The dependency proposed and used in EMU, modifies s_0 to depend on $s_{\min}$, the minimum non-positive stretch among all bonds (i) connected to the two nodes linked by the current bond:

$$\widetilde{s_0}(t) = s_0 - \widetilde{\alpha} s_{\min}(t), \text{ where } s_{\min}(t) = \min\{0, s_i\} \tag{12}$$

where $\widetilde{\alpha}$ is a constant typically chosen as 1/4, s_i is the bond strain for bonds with the index i going over all of the bonds connected to one of the two nodes linked by the current bond. Thus, the critical stretch s_0 on an extended bond (recall that only extended bonds are allowed to break) increases if any nearby compressed bonds exist.

We also note that the critical fracture energy used here is independent of the crack speed. For further discussion about this selection and its relation to the limiting crack speed, please see (Bobaru and Zhang 2015).

For the time integration we employ the Forward Euler scheme. A time step of 27.6 ns is stable for the finest discretization used in this paper based on the stability criterion established in Silling and Askari (2005), and this time step is used in all of the computations.

To prevent material interpenetration, and implicitly account for contact, EMU (Silling 2005) uses short-range force between nodes. The magnitude of the short-range force between nodes is defined as:

$$f_{\text{short}}(y_j, y_i) = \alpha_{\text{force\_fac}} \times c \times (\|y_j - y_i\| - D_{\text{contact}}) \tag{13}$$

where c is the elastic constant of the peridynamic bond, $\|y_j - y_i\|$ is the current separation distance between nodes i and j. D_{contact} is the distance where the repulsive force becomes active. This interaction distance is defined as:

$$D_{\text{contact}} = \min(\alpha_{\text{dist\_fac\_norm}} \times D_{\text{nom}}, \alpha_{\text{dist\_fac\_init}} \times D_{\text{init}}) \tag{14}$$

here D_{nom} is the nominal contact distance, equal to twice the larger of the node radii, and D_{init} is the initial separation distance between the two nodes in the reference configuration. The parameter $\alpha_{\text{dist\_fac\_norm}}$ determines how close nodes that are initially separated by a large distance are permitted to get before short-range forces are activated. Parameter $\alpha_{\text{dist\_fac\_init}}$ equals one plus the compressive strain at which the short-range force become active. Here we choose $\alpha_{\text{dist\_fac\_norm}} = 1.35$ and $\alpha_{\text{dist\_fac\_init}} = 0.9$.

For the spatial discretization, we perform convergence studies (see the Appendix), and based on those, the horizon size selected for the results subsequent to the convergence studies is $\delta = 0.9045$ mm, and a grid spacing $\Delta x = 0.225$mm (resulting in the value $m = \frac{\delta}{\Delta x} = 4.02$), leading to a grid of 452 by 452 by 16 nodes for the glass plate and 452 by 452 by 14 nodes for the backing plate. The meaning, selection, and use of peridynamic horizon and its relation to crack branching in brittle materials is discussed in Bobaru and Hu (2012). The reasons for using non-integer m values are due to the properties of the numerical integration algorithm. The numerical quadrature improves for values slightly larger than 4, for example (see Hu et al. 2010).

The impactor is considered as rigid (spherical), see Sect. 2. The Coulomb model is used for the friction between the impactor and target, with the Coulomb friction coefficient chosen as 0.2:

$$F_{\text{friction}} = \mu F_N \tag{15}$$

where F_N is the normal force exerted by the impactor's surface on a node. We do not consider a friction force for self-contact, but this can be added to the short-range normal force mentioned above.

4 The evolution of fracture and damage

While a more in-depth study could use statistical information from, e.g., tens or hundreds of experimental tests and quantify the number, size, and distribution of various fragments, the length of various crack systems (circumferential cracks, radial cracks, etc.), this was not possible here. Instead, here we aim for a qualitative analysis of failure modes and a direct comparison with experimental data from the single experimental sample shown in Fig. 1. For instance, we monitor the patterns for the circumferential and radial cracks, the number and locations of cracks parallel to the sides of the plate, the extent of the Hertz-cone crack, and number of major fragments. For such measures we are, in some cases, able to provide a more quantitative analysis, e.g., the location of the circumferential cracks and the extent of the Hertz-cone crack. The analysis below allows us to understand the likely causes for the many crack systems that develop in the sample. More specifically, we will identify, computationally, which wave interactions lead to the development of a particular crack system. This will shed light, for example, on the presence of the wispy lines

noticeable on fragments near the end of the Hertz-cone (see Fig. 4 below). Given the cascading effect of damage evolution in brittle fracture and its sensitivity to interactions with stress waves, a match between the computed results and the experimental observations cannot happen unless the dynamics of wave propagation and fracture evolution are correctly captured by the computational model.

4.1 An overview of damage evolution

In this section, based on the peridynamic computational results, we first give an overview of how damage evolves in the glass plate and then discuss in detail each type of crack system. As seen from Figs. 5 and 10, damage in the glass plate evolves as follows (see also the nodal damage index maps in Movie 2, showing it over the strike face of the glass plate, Movie 3, over the back face, and Movie 4, over a transverse cross section through the impact location):

- At around 3 μs after the Moment of Impact (abbreviated from here on as the MOI), two ring cracks around the impact location are seen on the top surface, and the Hertz crack cone has advanced about mid-way through the thickness of the glass plate, while on the bottom surface, an "asterisk" - like crack grows (see also Bless and Chen 2010) and expands laterally as well as advances upward through the thickness.
- After about 7 μs, radial cracks have propagated on the top surface while due to the reflection wave from the bottom, the Hertzian cone is deflected and starts to propagate almost parallel to the strike surface. Some of the radial cracks are now seen on both strike and bottom glass faces, and therefore it can be concluded that they are through thickness cracks (this will be confirmed later by the 3D plots of damage only, see Movie 5).
- After about 15 μs, new systems of cracks appear parallel to the sides of the plate, first on the bottom face parallel to the right side (closest to the impact region) and then cracks parallel to the up and down boundaries. More ring cracks form around the impact region on the strike surface.

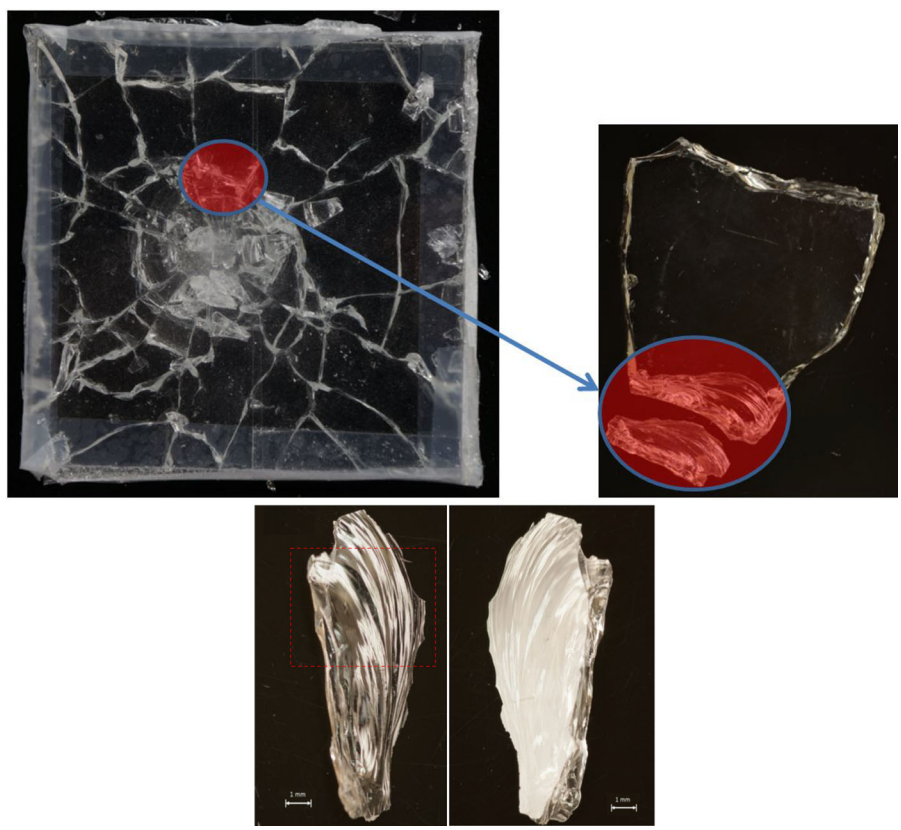

Fig. 4 Top left: bottom view of glass plate; top right: glass fragments from the region near the impact location; bottom left: the roughness of glass chip on the face corresponding to the surface of the end of the Hertz-cone crack; the fine lines are not cracks, but fine "ridges" on the surface of the Hertz-cone crack; bottom right: the side of the glass chip corresponding to the back side of the plate, showing an intact surface and the light reflections coming from the ridges on the other side of the chip

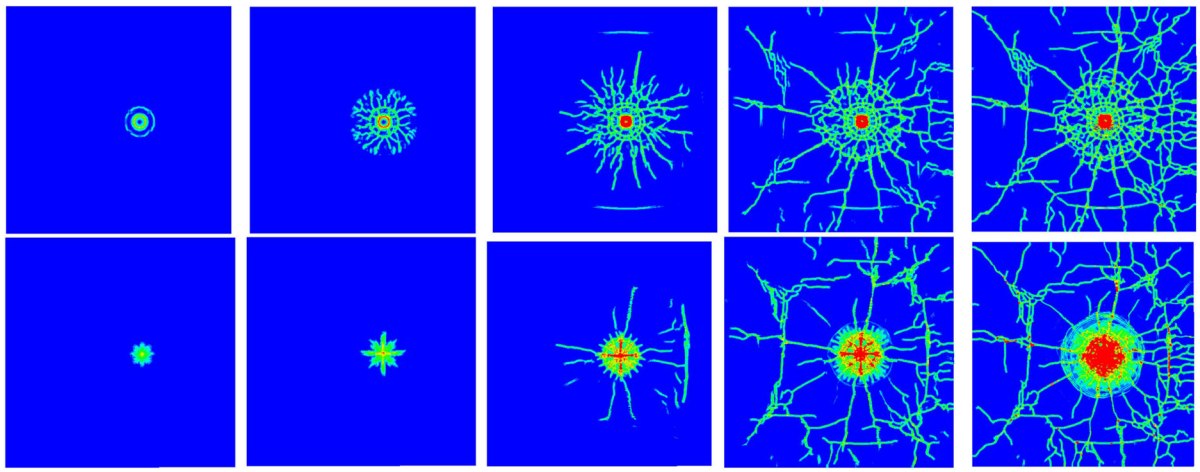

Fig. 5 Damage index maps (for $\delta = 0.9$mm) for the strike surface (top row) and the back surface (bottom row) of the glass plate, at the following times: 3.95 μs, 7.25 μs, 15.5 μs, 30.35 μs, 99 μs, all measured from the MOI

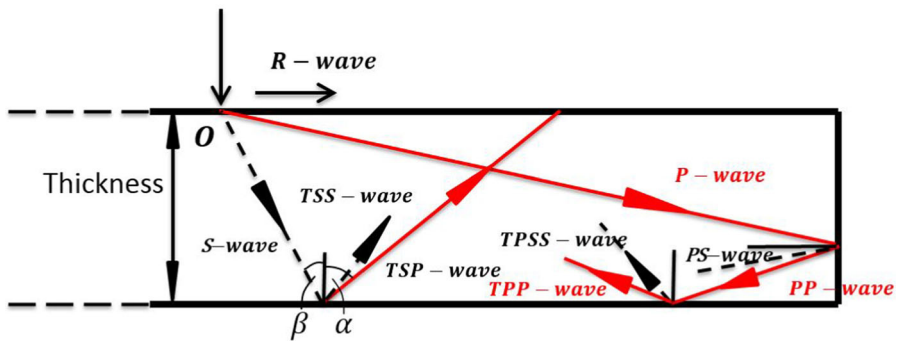

Fig. 6 Names assigned to some incident and reflected waves used in the paper

- At about 30 μs, crack systems are joining together and fragmentation in certain areas ensues. Some fine, wispy circumferential damage lines show up at about 1–2 cm away from the impact region and only on the back face of the glass plate. Boundary cracks appear to be moving from the sides, inward. Similar to what is seen in the experimental results, the boundary crack and fragment densities are significantly larger for the side of the glass nearer the impact location, than for the side that is farther from the impact location.
- From this time until 99 μs after the impact, the only damage that forms is that represented by coalescence of radial cracks, cracks starting from the boundaries, and circumferential cracks, the continued formation of very fine circumferential damage lines on the back surface, and the continued fragmentation of glass at the bottom of the Hertz cone. Some crack systems mimic the asymmetry of the impact location, indicating that they are a result of waves being reinforced/interacting with waves reflected from the side boundaries of the sample. This is observed for cracks parallel to the sides, as well as the fine circumferential damage on the bottom face.

Note that in the experiment, due to the taping of the backup PC plate to the glass plate along their edges, some extra damage will happen due to the subsequent rebound of the PC plate onto the glass. For instance, the cracks parallel to the sides may continue to grow, and we see this in the post-mortem sample, see Fig. 1. Since in the computational model the PC plate is not taped on its sides to the glass, we do not expect to obtain damage induced by the bounce-back of the PC plate, even if we let the code run past the 99 μs mark.

In the following sub-sections, we describe in detail how the computational results help us understand the formation of the first two ring (or band) cracks on the

top face, the Hertz cone crack evolution, the growth and propagation of radial cracks, the systems of cracks parallel to the sides of the plate, the boundary cracks growing inwards and "fake branching" of radial cracks, and the fine damage lines seen on back surface of the glass plate. Waves interaction and reinforcements are the cause of the damage and cracks in the plate. In order to shorten the writing, we abbreviate the names of different types of waves as follows (see Fig. 6): the incident longitudinal, shear, and surface waves are named the P-, S-, and R-wave. The pressure (shear) component of the reflected P-wave is named PP-wave (PS-wave); similarly, the pressure (shear) component of the reflected S-wave is named SP-wave (SS-wave). The Rayleigh wave generated by the P-wave reflected from the strike and back glass surfaces is named the PR-wave. The shear component of the through-thickness reflections of the PS-wave will be called the TPSS-wave, the through-thickness reflections of the S-wave will be called the TSS-wave. Note that the through-thickness reflected waves are Lamb-type waves. In Fig. 6, we draw some of these waves.

4.2 Ring or band cracks near the impact point

The first type of cracks that forms (besides the initiation of the Hertz-cone crack, discussed in Sect. 4.3) in the glass plate soon after impact is a set of two clearly identifiable ring cracks (or band cracks) on the top surface of the plate (see Fig. 5). These cracks are different from the first ring formed on the top surface that is caused by the contact forces with the sphere (the initiation of the Hertz-cone crack). Similar bands are seen in the results given in Hu et al. (2013), where a frame was used to hold the two plates. In this section, we explain the causes for the generation of these cracks and discuss how well the PD model predicts them.

The explanation for the ring (band) cracks forming around the impact region in brittle plates has been given in a paper in 1964 by Bowden and Field (Bowden and Field 1964). This paper discussed differences in the modes of brittle fracture of solids impacted by liquid, by solid, and by shock. One cause for the observed differences between the modes of fracture generated by these types of loading is the difference in the intensity and duration of loading: 1 μs or 2 μs in the case of liquid, and tens to hundreds of microseconds in the case of impact with a solid. For low impact speeds, of just meters per second, the contact between the projectile and the target can be as long as 100 μs, while for higher impact speed, of ≈ 100 m/s or higher, the rebound happens in less than 10 μs (see Hu et al. 2013). This is the reason for which dynamic solid impact at low speeds leads to fracture similar to that caused by "static" loading methods.

In reference (Bowden and Field 1964), particular attention is paid to fracture in *thin plates*. The authors of Bowden and Field (1964) perform experiments and provide explanations for the formation of band or ring cracks on the impact surface of the thin plate. The mechanism that leads to these cracks is wave reinforcement. The passing of the body waves (longitudinal and shear) do not create conditions for crack formation on the top surface. The surface wave propagates along the strike surface at velocity C_R, while the two body waves travel into the plate with velocities C_1, and C_2, as shown in Fig. 7. The P-wave reflects from the bottom surface and produces PP- and PS-waves components (see Fig. 8). Where the PP-wave meets on the top surface with the R-wave, wave reinforcement happens and it leads to tensile stresses larger than the critical stress to initiate fracture. Further sets of ring cracks could, in principle form, by continued reflections from the top and bottom plate surfaces, but wave attenuation caused by energy dissipation via fracture, as well as wave dispersion, limits this possibility. The second ring forms when and where the PS- or SP-waves meets and reinforces the R-wave traveling on the strike-face of the plate.

Based on simple wave propagation calculations on the geometry shown in Fig. 7, Bowden and Field compute the dependence of the outer radius of this first band/ring crack as a function the plate thickness. Their experiments with *liquid impact* match closely these

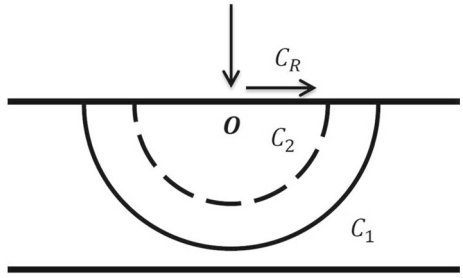

Fig. 7 Point load on a plate, showing the propagation of the different elastic waves (redrawn from Bowden and Field 1964)

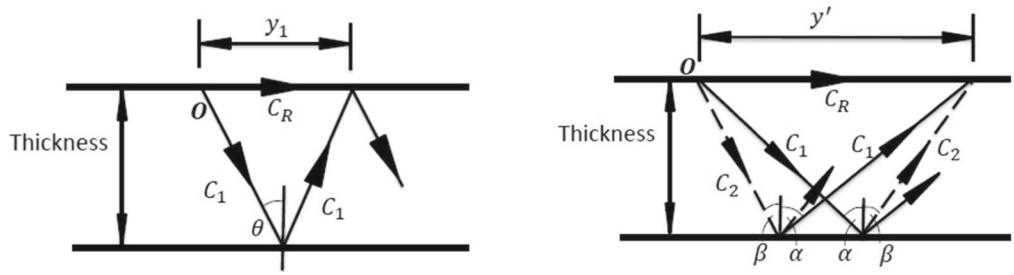

Fig. 8 Left: The forming of first damage band by wave reinforcement; Right: The forming of second damage band by wave reinforcement (redrawn from Bowden and Field 1964)

analytical calculations (see Fig. 9) that show a linear dependence of the radius of the ring cracks with the plate thickness.

For the glass plate thickness in our problem (3.3 mm) and the wave speeds the peridynamic model computes (see Sect. 2), we have a ratio $\frac{C_1}{C_2} = 1.732$. Using similar calculations as in Bowden and Field (1964), the analytical model for wave propagation in the thin glass plate gives a radius of the first ring crack of $y_1 \approx 4.13$mm (for an incident angle $\theta = 32.05°$, see Fig. 10). The surface wave meets the PP-wave at around 1.38 μs. For the second ring, based on the data used in the computational model, the analytical value of the second ring crack is $y_2 \approx 6.51$ mm. The waves meet and reinforce on the surface at around 2.71 μs. These values are computed based on a simplifying assumption that the impact region is a *geometrical point*. See (Bowden and Field 1964) for a detailed discussion on adjustments due to a finite width of the region of impact (and for liquid impact).

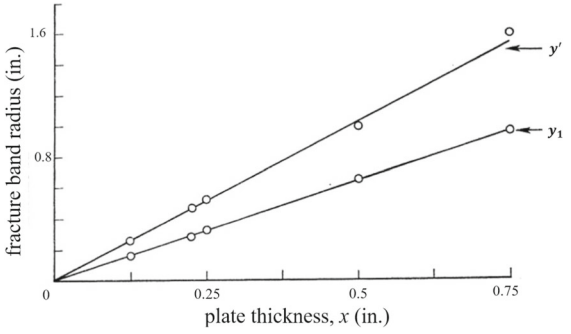

Fig. 9 The radius of the first and second damage rings/cracks plotted against glass plate thickness (from Bowden and Field 1964). The lines are from the analytical relationship based on elastic wave propagation generated by point-impact, while the empty circles are data from experimental measurements of *liquid impact* in (Bowden and Field 1964)

The peridynamic simulation results in Fig. 11 show that the first ring crack has a radius of about 4 ± 0.2 mm, with the $\pm$ sign used here because of the discrete character of the grid spacing in computations. Most of the nodes that are under the black circles drawn on top of the computational results have a damage index of around 0.3–0.4 (blue-green color), which indicates the presence of a crack. Indeed, for a relatively coarse discretization (relative to the horizon size), a straight crack passing by a node leads to a nodal damage index smaller than the theoretical 0.5 value obtained in the limit of the discretization size going to zero. A 0.3–0.4 nodal damage index value for nodes on the surface of a straight crack is to be expected when a $\delta/\Delta x$ value of around 3 or 4 is used in 3D. Notice also that the thickness of the first band cracks is in the same range as the width of the impact region (see Fig. 11). This is what Bowden and Field suggested in their analysis of solid impact. The second band crack (see Fig. 10a, b) starts to form around 2.85 μs and is fully formed at about 4.125 μs at a radius 6 ± 0.2 mm away from the impact center. These results match remarkably well the analytical calculations discussed above.

The inner yellow–red ring in Fig. 11 is the location where Hertzian-cone crack starts. This crack forms because of direct contact forces with the impacting sphere. The radius of the Hertzian-cone damage ring is about 2.5 mm, the mark of this ring can also be seen from the cross-section plots shown in Figs. 10 and 12. The Hertz-cone crack continues to grow through the thickness and radial cracks also start propagating in the in-plane direction. Observe that on the bottom face of the sample (see bottom row of pictures in Fig. 5), radial cracks are the first ones to develop. One question to be answered is why radial cracks are forming after the band cracks on the strike face, but are

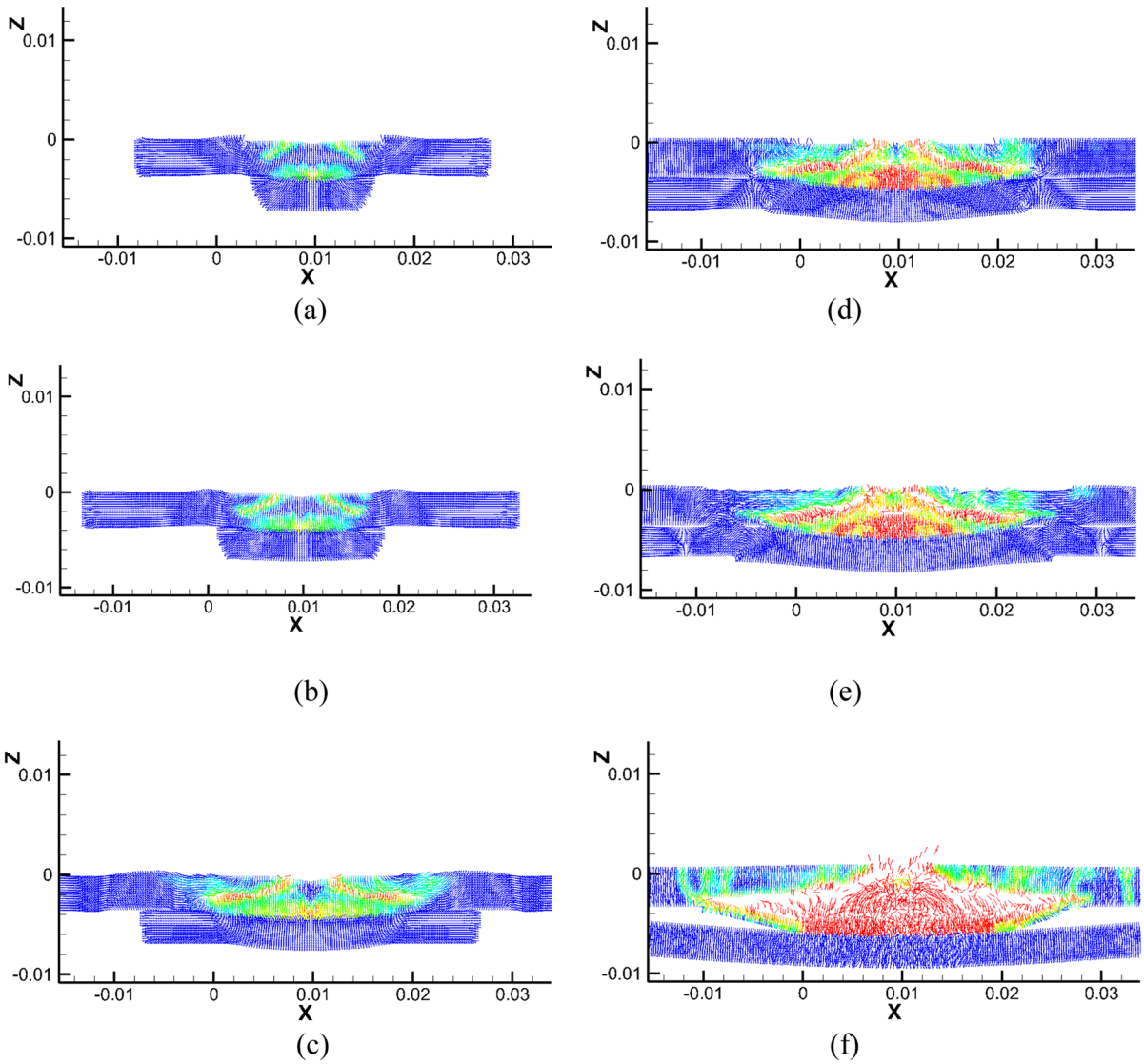

Fig. 10 Damage and nodal velocities (in the *xz*-plane) for a portion of the cross section of glass plate at: 2.71 μs, 3.54 μs, 6.84 μs, 11.23 μs, 14.54 μs, 99 μs after the MOI. Only nodes with non-zero *xz*-velocity are shown. Units here, and in the rest of the paper where the *xyz*-coordinates are shown, are in meters

the first to show up on the back face of the glass plate? The answer to this question and the Hertzian-cone crack are discussed in the next two sections.

To confirm the failure mechanism that leads to the formation of the first and second damage bands, we perform another computational test on a thicker plate (5.0 mm). According to the experimental results in Fig. 9, the damage bands radii should increase linearly with the glass plate thickness. In Fig. 13, the computed damage on the thicker plate top surface is shown relatively soon after impact, before the ring cracks fully develop because by then damage is spread over the entire region, making it harder to see these ring cracks. We again mark the theoretical locations for the first and second ring cracks by drawing them as red circles using the corresponding radii for this plate thickness.

In Fig. 13, the radius of second damage band computed by the peridynamic model is 10.5 mm in the 5 mm thick glass impact. The analytical value is about 10 mm. The first ring-crack radius based on the analytical calculations should be about 6.25 mm, and

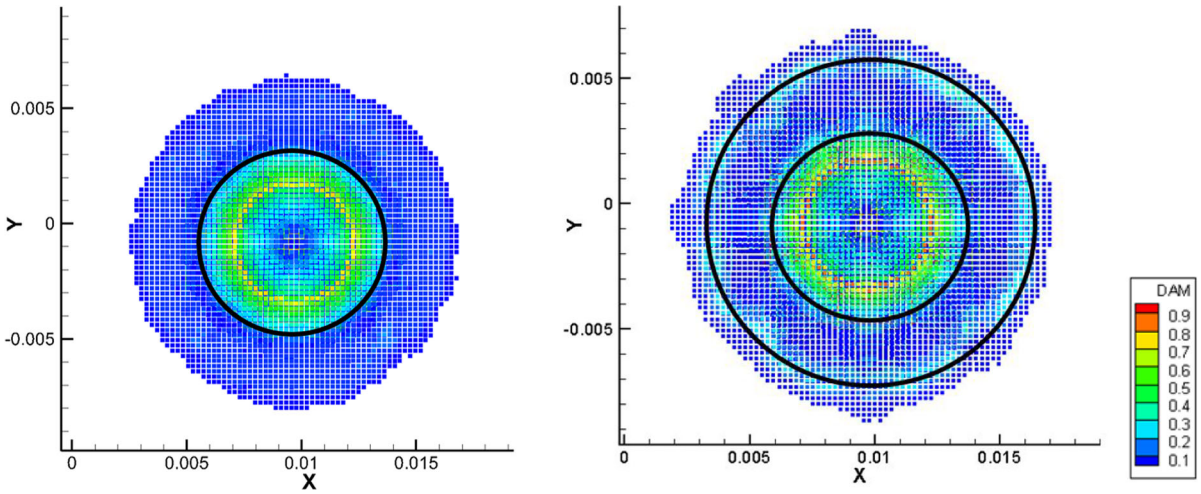

Fig. 11 The top view of first and second damage bands (left: at 1.61 μs after MOI; right: at 4.125 μs from MOI). Only nodes with non-zero damage on the strike face are shown. The black-line circles are drawn on top of the simulation results using radii given by the analytical formulas from (Bowden and Field 1964) for point impact. The ring caused by the contact (Hertz-crack) is seen inside of the first damage band

the early stages of the formation of a ring-crack of radius about 6 mm can be distinguished from the damage plot in Fig. 13. Deviations from the results shown in Bowden and Field (1964), and reproduced in Fig. 9, are expected because those results are obtained from experiments with liquid impact, whereas in our simulations we use impact with a solid (and rigid) sphere. The inner damage ring (with damage index around 0.9 in Fig. 14) is the Hertzian-cone crack, see Fig. 14. The significant Hertz-cone crack growth due to the sphere impact influences the wave propagations responsible for the band cracks discussed above.

4.3 The growth of the Hertzian-cone crack

In this section we discuss the growth and propagation speed of the Hertz-cone crack. As seen from Figs. 10, 12, 15 and Movie 6, there are several stages in the evolution of the Hertzian crack characterized by changes in the crack path and propagation speed. In what follows we connect the cone-crack path and its propagation speed, with wave interactions (see results given in Figs. 12 and 15).

To find the propagation speed for the Hertz crack from the PD results, we first determine, approximately, the crack tip location by observing, from the damage maps in Fig. 12, the coordinates of nodes around the cone-crack front, which have a damage index of at least 0.4. The cone-crack in the XZ plane is monitored from Fig. 15, where we track the cone-crack tip with damage index of at least 0.4 in "manual" post-processing of results (see below). We monitor nodes with this particular damage index because, while, in theory, if a straight crack passes by a node (the node is on the crack surface), that node's damage index is 50%, due to the discretization and depending on how fine that discretization is relative to the horizon size, that crack-surface node's damage index will be lower than that. Choosing 40% as a threshold seems like a good compromise: it is high enough to ensure the monitored node is sufficiently close to the crack surface and is low enough to ensure that even when using a relatively coarse grid (an m-value of 4 or 5) we do not miss nodes that are on the crack surface.

This "crack-tip" location, estimated for all data-dump times (performed every 0.1375 μs), is used to compute the average crack speed using forward differences:

$$v(t_i) = \frac{\sqrt{(x(t_i) - x(t_{i-1}))^2 + (y(t_i) - y(t_{i-1}))^2 + (z(t_i) - z(t_{i-1}))^2}}{\Delta t} \tag{18}$$

where t_i are times of data dumps, $v(t_i)$ is the crack tip speed at t_i. A running average over 1.0 μs time-

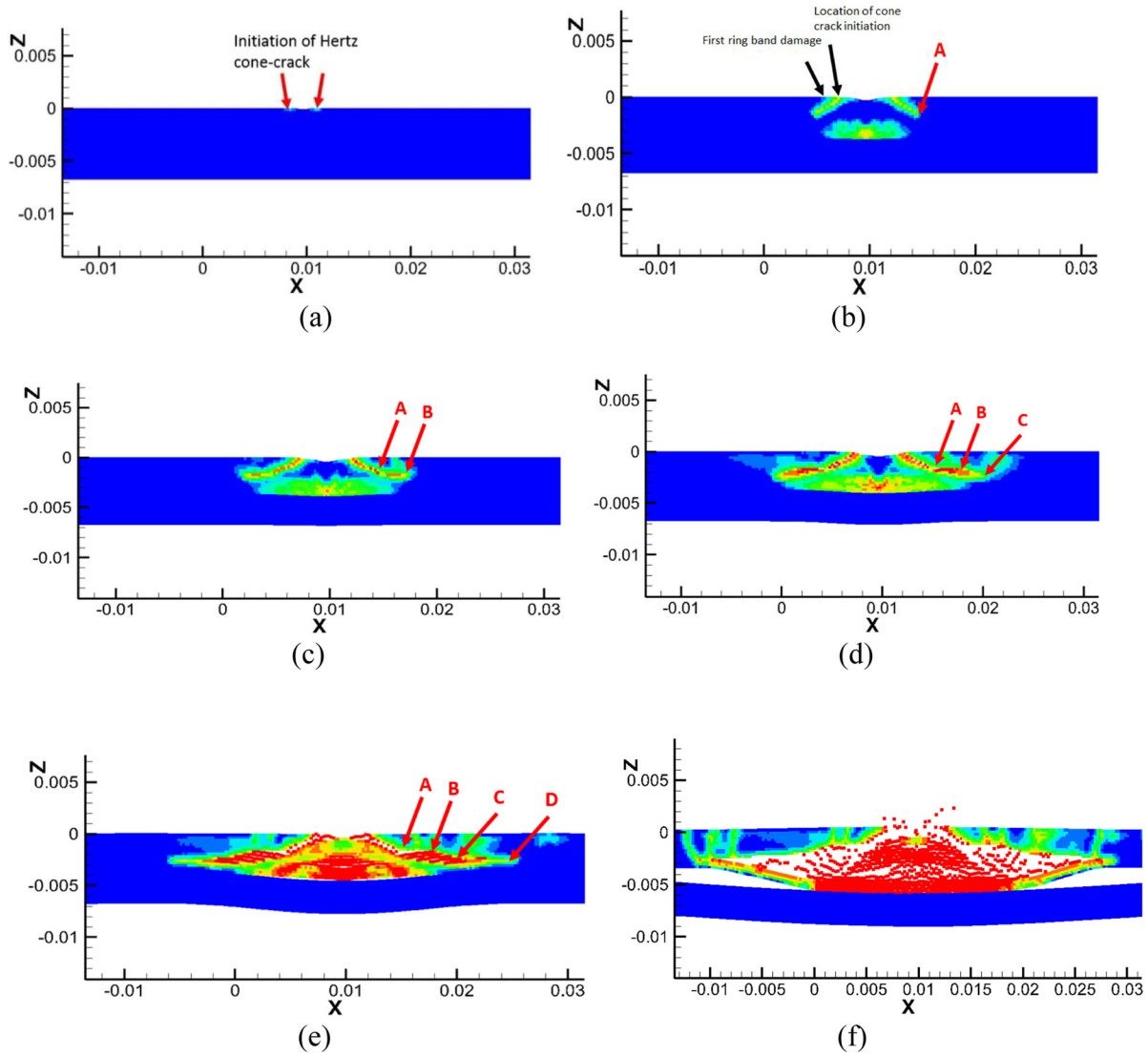

Fig. 12 Damage maps for part of the cross-section through the point of impact showing the initiation of the Hertzian-cone crack at 1.61 μs in (**a**), the first ring band and the cone crack at 2.715 μs in (**b**), the deflection of the cone crack into a plane parallel to the strike face at 3.81 μs after MOI in (**c**); cone crack tip reaches point C at 6.84 μs in (**d**), and grows to point D at 14.54 μs in (e). In (f), damage map at 99.0 μs after MOI

intervals is used as a low pass filter to smooth the velocity data. The equation of the running average is:

$$V_{\text{average}} = \frac{V(t_{i-n}) + \cdots + V(t_{i-1}) + V(t_i) + V(t_{i+1}) + \cdots + V(t_{i+n})}{2n+1} \tag{19}$$

where $2n + 1$ is the number of data points over which the average is run. Here we used $n = 3$, which provides a good balance between excessive noise and too much smoothing that would erase the stop-and-go behavior observed for this crack past the 15 μs mark from the MOI (see Fig. 12). Depending on the plane in which the propagation speed is computed, dependencies on the y-coordinate (for the XZ-plane), for example, drops from Eq. (18).

The different speed stages in time, over the first 26 μs from the MOI, for the cone-crack tip are marked as A, B, C, D at the time locations shown in Fig. 15. The time stamps A, B, C, D in this figure correspond to the crack tip locations shown in Fig. 12.

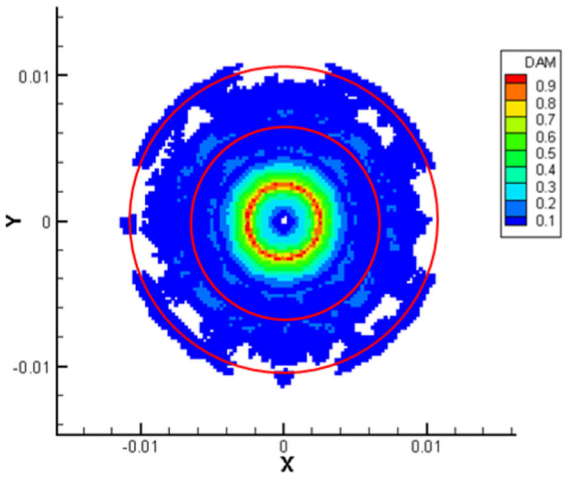

Fig. 13 Damage map (the undamaged nodes have been blanked) at 6.6 μs after MOI for strike face of a thicker plate (5 mm). The analytically calculated (for point impact) first and second ring-cracks are shown by red-line circles drawn on top of the PD-computed nodal damage map

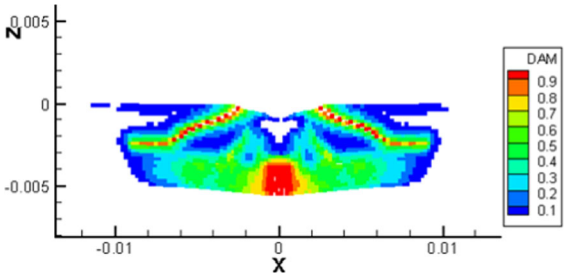

Fig. 14 Damage index map for the cross section of the 5 mm thick glass at 6.6 μs after MOI. Undamaged nodes are blanked

The Hertzian-cone crack starts to propagate along the maximum tension direction in the material (Hertz 1881) at a speed of about 3000 m/s (see point A), close to the Rayleigh wave speed but only for a short time (less than one microsecond). Such high crack propagation speeds are not normally seen in non-crystalline materials, where crack speeds top at around $0.66\times C_R$ (see Table 11.1 in Ravi-Chandar 2004). Experiments that measure the crack speed for cracks generated by impact during the early stages of their propagation are not easy to conduct. Given that when cracks are constrained in their growth (like in crystalline materials) cracks do propagate with speeds even as high as $0.9\times C_R$ (see Table 11.2 in Ravi-Chandar 2004), it is plausible that in the early stages of impact, under the intense loading, Hertz crack could grow as fast as shown by our computations. Similar conclusions have been drawn in Bobaru and Zhang (2015). At the same time, the first few values shown in Fig. 15 may be affected by the approximate way in which we compute the propagation speed (see above and also Zhang et al. 2018). Note that a 2D measurement of the crack speed for a 3D crack can influence the interpretation of the result.[1]

At this moment, the cone-crack angle (the angle between cone crack and the load surface) is about 31°. For soda-lime glass ($\upsilon = 0.22$), the experimentally measured Hertzian-cone crack angle under static loading is 22° (see Chaudhri 2015; Chaudhri and Chen 1986; Field 1988). Note that this behavior, of increasing cone-crack angle with increasing impact velocity, is observed in many brittle materials: see (Kocer and Collins 1998), reference (Field et al. 1989) for ceramics (cone crack angle is 28° at the impact velocity of 40 m/s and about 48° at 90 m/s) and reference (Field 1988) for glass ceramics (cone crack angle is 35° at the impact velocity of 60 m/s and 55° at 350 m/s). Explanations for the difference in cone-crack angle between static and dynamic loading are given in Field (1988) (see also Kocer and Collins, 1998).

At point A in Fig. 12, the crack changes direction and grows almost parallel to the strike face. For the run from A to B, the crack slows down to about 2000 m/s. Wave reflections are responsible for both the change in direction and the propagation speed. From B to C (see Fig. 15) there is another precipitous drop in propagation speed with only a slight change in direction. Continuing from C to D, the propagation speed reaches a plateau and stays at an almost constant value of around 700 m/s. The crack path during this stage is only slightly tilted towards the bottom of the plate, getting close to breaking through and forming thin glass chips on the back face. In experiments that used tungsten carbide (WC) spheres impacting on soda-lime-silica of dimensions $50 \times 40 \times 10$ mm (see Chaudhri and Chen 1986), a similar behavior of the cone-crack is observed: initial growth at an angle with the loading direction, which later bends and follows a

[1] Imagine breaking a chocolate bar by bending it: the crack grows through the thickness of the bar with a finite speed, but if exclusively viewed from the plane of the bar, the crack would appear to "grow" in an instant, thus have an infinite propagation speed! This effect is not at play here since we are measuring in a plane in which the crack indeed advances.

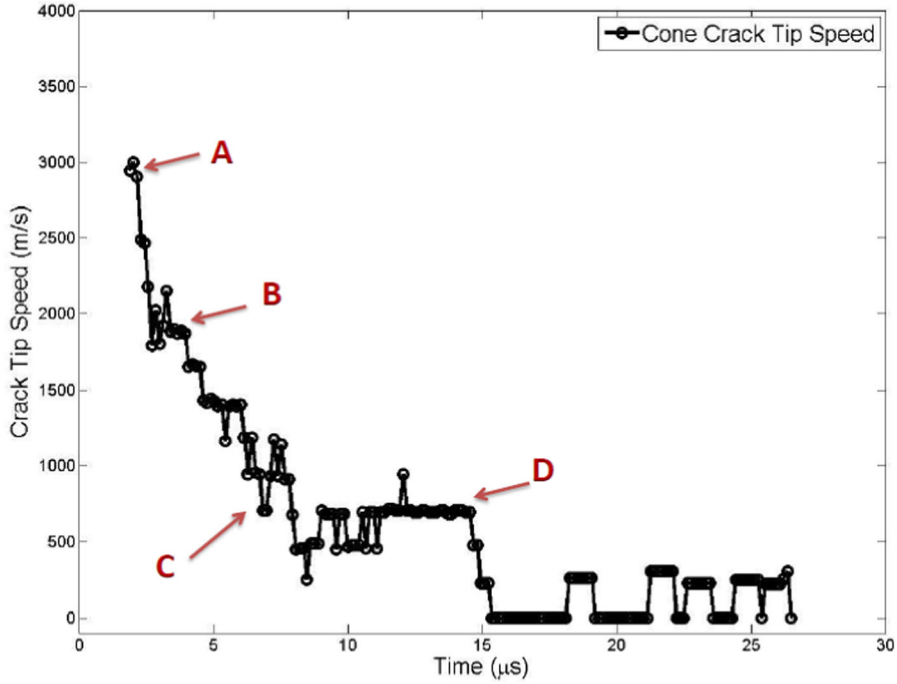

Fig. 15 The cone crack propagation speed measured in the XZ plane

direction almost parallel to the impact surface. The maximum crack growth velocity observed in Chaudhri and Chen (1986) is 1800 m/s through the tensile zone, but when the crack reaches the "compression zone", the velocity drops to around 200 m/s, and it remains nearly constant for several microseconds as the crack approaches the back surface. In our thinner plate, the cone-crack goes through a brief speed plateau at point B, a more significant one from point C to D, with the crack speed staying at about 700 m/s, before a "stop-and-go" region beyond location D.

After location D in Fig. 12 or around 15 μs from the MOI, the Hertzian-cone crack grows surprisingly slowly, in a "stop-and-go" fashion, with average speeds not reaching above 200 m/s. This behavior is caused by a PS-wave, which would take about 14.8 μs to reach the location of point D, when it is bouncing back from the right boundary (the closest to the impact location). The damage observed in the PD results for the late stages of growth of the Hertz-cone crack is discussed in the next section, where we explain the reasons for the presence of the wispy circumferential lines seen in the last plot, bottom row, of Fig. 5.

Notice that Fig. 12 shows that, concomitant with the growth of the Hertz-cone, damage evolves on the bottom of the plate as well. The initiation of radial cracks on the bottom face of the plate is in the form of an asterisk-like feature (see first figure on bottom row in Fig. 5). This damage is caused by waves "splashing" onto the back face of the plate causing large hoop-stresses on that surface. As seen from Fig. 16, damage starts as isotropic on the back face and it grows (radially) very fast, after which the cracks localize and continue to grow at a much reduced speed. The "initial asterisk" appears to have twelve hands, but some of the branches are left behind and/or swallowed by others, and only eight-sided asterisk survives and continues to grow (see Movie 7, left: the bottom radial cracks propagation with all nodal velocity vectors, the length of the arrow represents the magnitude of nodal velocity; right: where all nodal velocity vectors shown have a fixed length independent of their magnitude, for better visualization).

In our computations, the localization of this damage type is a result of the broken symmetry caused by imperfect isotropy of the discretization (Dipasquale et al. 2016). Moreover, because the numbers in the nodal coordinates are not symmetric about the impact point, we will also have asymmetric build-up of round-off errors that can influence fracture (Ha and Bobaru 2011a) asymmetry. Plus, when waves reflect from the sides of the sample, because of the asymmetric impact,

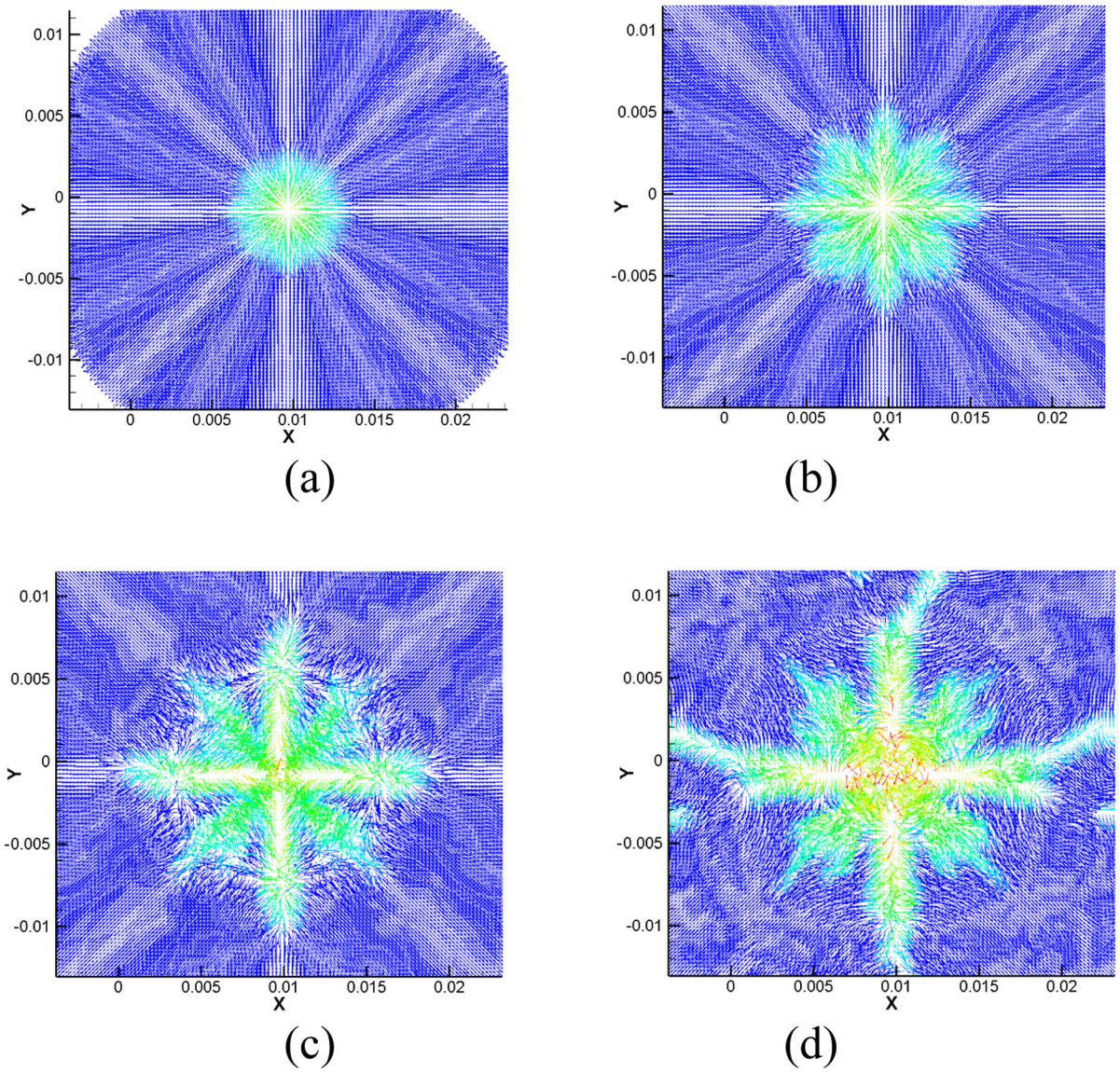

Fig. 16 The nodal velocity vectors for nodes on the back face of the glass plate (at 2.03 μs, 3.68 μs, 6.01 μs and 7.8 μs). The colors indicate the damage index. All velocity vectors are scaled here to unit magnitude, for better visualization. See Movie 7 for the actual velocity magnitudes corresponding to this case

they further destroy the symmetry of crack growth. Mathematically speaking, symmetry should not break and any failure of this type should happen simultaneously in all of the bonds on a circumference. In the actual material, defects and minor heterogeneities lead to localization of failure. While the uniform grid used in our computations may influence the number of arms for the "star-shaped" damage, such influence is not major because results in other impact problems with an unstructured grid (see Henke and Shanbhag 2014) are very close to those with a structured grid and an *m*-value of 4 used in our computations.

The asterisk-type cracks at the bottom of a plate have been reported in impact experiments on glass before (see Bless and Chen 2010) and we also observed them in earlier computations (see Bobaru et al. 2012). The resulting radial crack/damage growth advances in two ways: on the back face and through the thickness (from the bottom surface towards the Hertzian-cone crack). When these two crack systems

meet, profuse fragmentation ensues inside the Hertz cone region (see Fig. 12 and Movie 6).

4.4 Fine roughness/ridges on some crack surfaces

A zoom-in into the region of impact location is shown in Fig. 17 for both the experiments and the simulation results. The plot for the simulation results (Fig. 17a) uses the same scale as that in the experimental picture (Fig. 17b). The simulation results are of the damage on the back-face of the glass. In Fig. 17(a), in addition to the radial cracks, some fine circumferential lines of damage are observed. The region over which these lines extend around the impact point has roughly a diameter of 3.8 cm $\sim$ 4.0 cm, both in our experiments and the computations (see Fig. 17b). A slight asymmetry about the impact point is noticeable. This indicates the likely role played by waves reflected from the sides of the plate, since the asymmetry matches the asymmetry of the impact location: closer to the right boundary (as seen from the bottom face) and farther from the left boundary. It can be seen that the fine rings (with diameter of about 4 cm) that form on the bottom surface of glass (see Fig. 17a) are not through-thickness cracks since the damage levels are around 20 $\sim$ 30%. This observation is confirmed by the cross-section in Fig. 18. We can conclude that these fine lines of damage are in fact, signatures of roughness of the Hertzian-cone crack surface that cuts through, parallel to the bottom face, a few nodes above the back face. These nodes with partial damage on the back face of the plate do not have a crack passing through them, but a crack passes near them (the Hertz-cone crack) and that crack surface is rough (in the radial direction), so neighbors of such nodes have a slightly higher or lower damage index.

The roughness of the Hertz-cone crack is caused by sudden changes in the direction of the fracture plane, induced by wave interactions. In the simulation, the crack tip propagation speed for the Hertz-cone crack in this area (see beyond point D in Figs. 12 and 15) is around 250 m/s, when it is propagating. Observe that, in this region, the growth of the Hertz-cone crack is "stop-and-go". This is indirect evidence that stress waves play a major role here in determining the morphology of the crack surface. The Hertzian-cone crack between points C & D in Fig. 12, and especially after point D, grows very slowly and this makes it easier for any incident wave to influence its direction of propagation, resulting in a landscape of closely packed sharp ridges. These fine ridges are easily observed by analyzing the fragments from our experiment. In Fig. 4 we see that the actual glass chips that form on the back face towards the end of the Hertzian-cone crack present a very rough surface with such closely-packed ridges on the side corresponding to the Hertz crack surface, while the side corresponding to the back face is perfectly intact (no through-cracks).

A laser scan of the marked portion of the glass chip surface shown in the bottom left of Fig. 4 is given in

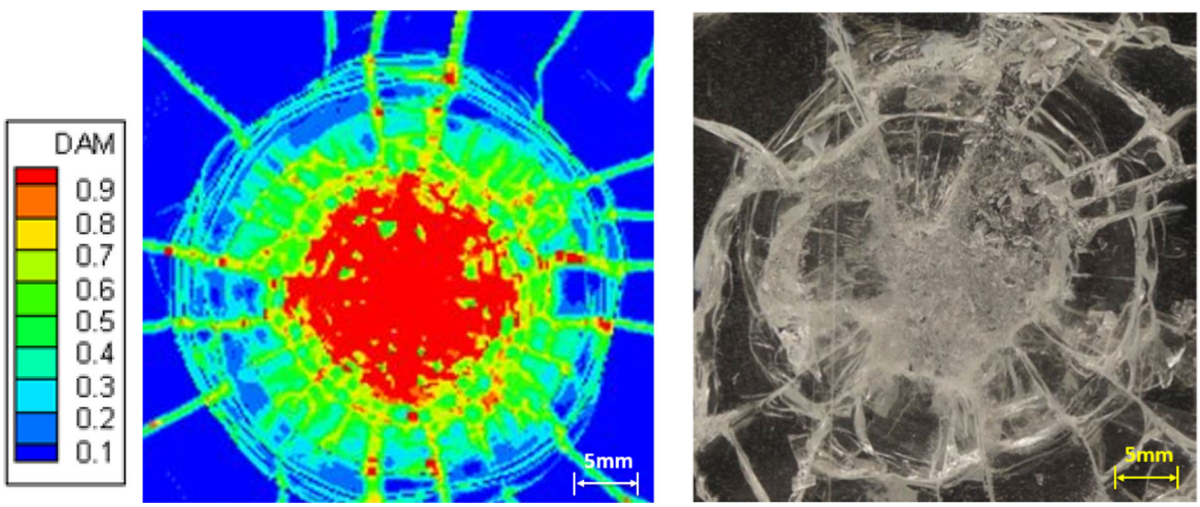

Fig. 17 Left: zoom-in on the computed damage map shown in Fig. 5 seen on the back face of the glass plate at 99 μs; Right: zoom-in (at the same scale as on the left figure) on photograph shown in Fig. 1 of the glass near the impact location

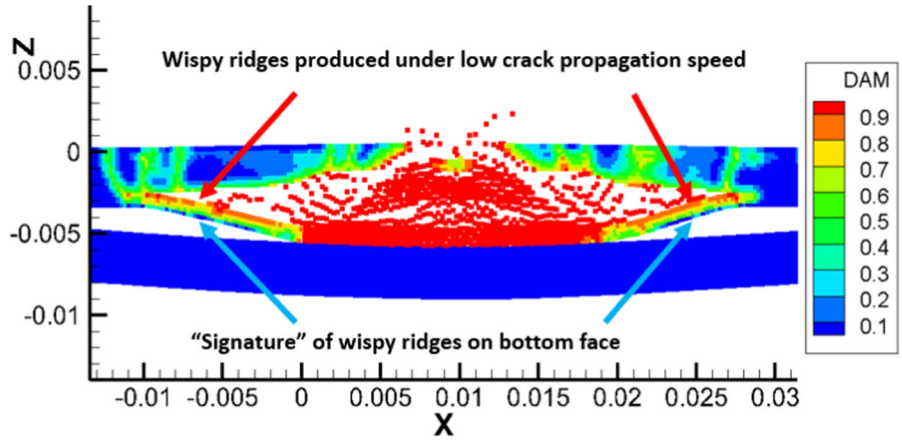

Fig. 18 Computed damage map for part of the cross section through the impact point at 99 μs

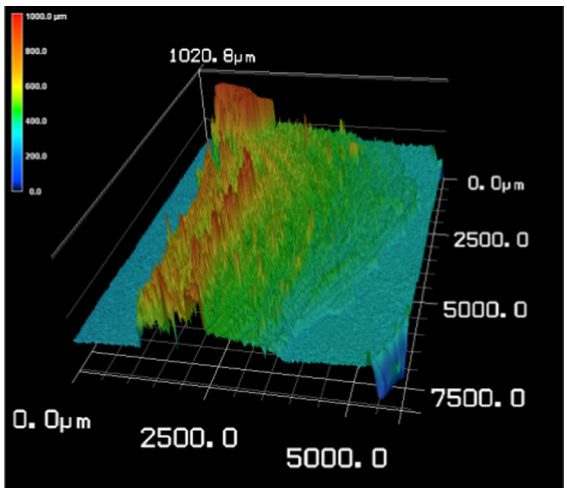

Fig. 19 3D surface roughness (obtained by laser scan) of the glass chip in the bottom left of Fig. 4. Area scanned is marked by the red square box in Fig. 4

Fig. 19. The laser wavelength is 405 nm, and the power is 0.98 mW. An objective lens of 5 × is used for scanning the fracture surface (∼ 5 × 7.5 mm^2). The sample is directly placed on the stage of the microscope in open air, at room temperature. The scan confirms that there are no through cracks in the chip, and that what appeared to the naked eye to be fine crack lines, are actually fine roughness on the crack surface that formed the glass chip.

In summary, after the Hertzian-cone crack reaches point D in Fig. 12, its propagation is intermittent (stop-and-go), with an average speed of around 42 m/s. The crack advances less than 3 mm over 85 μs, while before that point it crossed over 2 cm in less than 15 μs. During this late period the fine roughness is generated. Usually, rough crack surfaces are generated in dynamic brittle fracture when the crack runs at speeds close to the limiting speed, normally a value between 0.4 to 0.6 of the Rayleigh wave speed of the material. Here we found a case when crack surface roughness happens on a slowly advancing crack front because of wave interactions.

The picture that emerges from this study is the first evidence of a computational model capable of predicting roughness of crack surfaces that forms as part of an impact event. Not only is the roughness obtained by the numerical model at about the same locations as seen in the experiments, but we can now see how the roughness of cracks is induced by stress waves interacting with a slowly advancing transverse crack that is the end of the Hertzian-cone crack induced by the impact on the thin plate (see Movie 6). The resolution of our computational model here is not better than 225 μm (the grid spacing used). The thickness of the ridges seen on the glass chips from experiment (see Figs. 4 and 19) may be ∼ 50–100 μm. We also performed a test with a smaller horizon size and finer grid ($\delta = 0.6$ mm, and corresponding grid spacing of 150 μm) and the results seen in Fig. 20, show finer and more lines than with the coarser horizon size and grid (see Fig. 21). Obtaining the same behavior using several different horizon sizes (and discretization grids), confirms that the model captures the essence of the physical phenomenon responsible for these fine ridges (wispy circumferential lines) observed on the actual glass chips coming from the ends of the Hertz cone-crack. Being able to capture the main features of wave interactions present in this problem, independent of the PD horizon size,

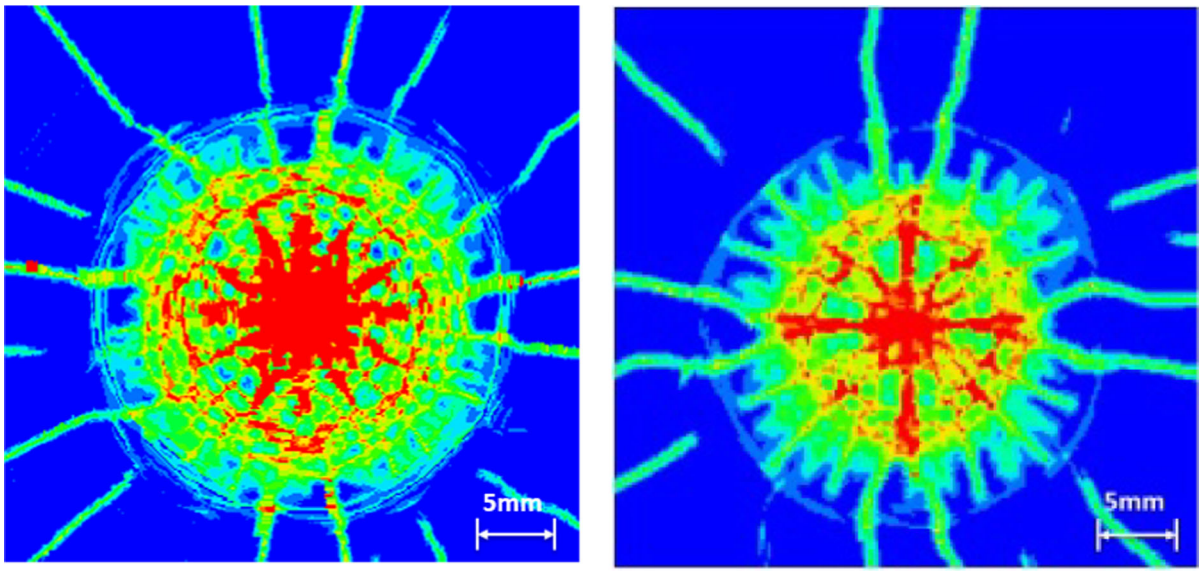

Fig. 20 Damage index map for nodes on the back surface of the glass plate, at 30.1 μs from MOI. Left: solution obtained with a smaller horizon ($\delta = 0.6$ mm, grid spacing of 150 μm); Right: zoom in on the central region of the corresponding plot in Fig. 5 ($\delta = 0.9$ mm, grid spacing of 225 μm)

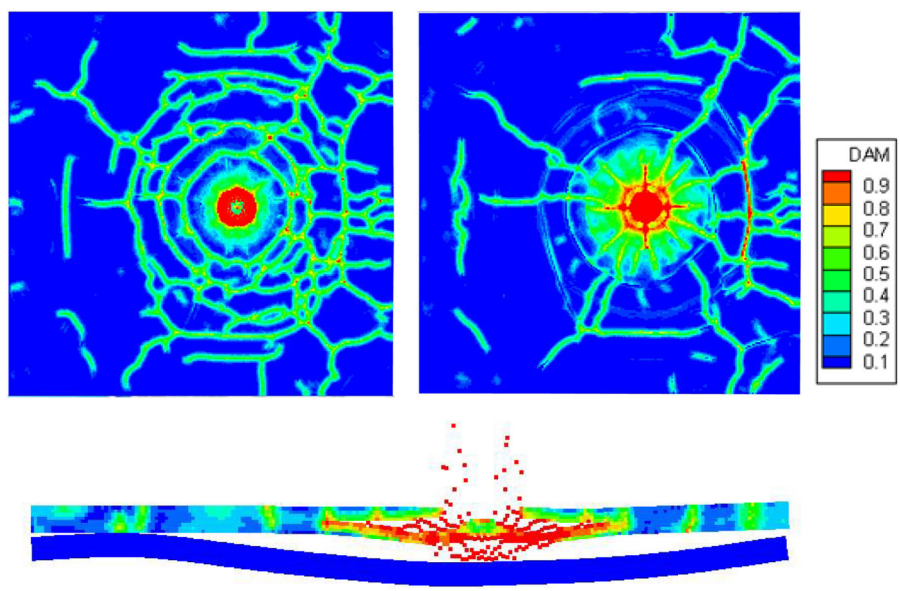

Fig. 21 Damage maps for $\delta = 2$ mm at 99 μs. Strike face (left), back face (right), and cross-section through the impact point (bottom)

relies on having a horizon smaller than a certain value that does not create artificially high wave dispersion due to the size of the nonlocality. Direct experimental evidence of the wave interactions creating the observed surface roughness on these glass chips may be possible in the future with further advances in experimentation technology.

4.5 The evolution of radial cracks

The simulation results show two different sources of radial cracks production (see Fig. 5): the bottom surface and the top surface. Soon after their initiation, these two sets of radial cracks merge (see Movies 5 and 8). The crack patterns seen in Fig. 5 show that during the initial stages, the radial cracks on top and

bottom faces are different, but later (beyond 15 μs from MOI) the radial cracks on the two faces correspond to each other, because of the merger.

The first radial cracks that appear are on the bottom face of the glass plate and these are caused by large hoop stresses induced by the "splashing" of the shear wave onto this surface (see more details in Sect. 4.2 and 4.3) and by the expansion of a damage "disk" on this surface. The damage disk localizes into a number of radial cracks that continue to grow. The mechanism for producing radial cracks on the top surface is slightly different simply because of the ring cracks formation (see Sect. 4.2) that precedes them and partially releases the hoop stresses. In what follows, we focus on:

a) Investigate how radial cracks initiate on the top surface,
b) Explain what sustains the radial crack propagation after their initiation stage.

To observe the initiation phase for the radial cracks on the top layer, we investigate the rectangular prismatic region highlighted in Fig. 22, close to the second damage band. By monitoring the bond strain, in time, for pairs of nodes whose bonds are aligned with the hoop, radial, and transverse directions, we see that the bonds along the hoop direction break first (see Fig. 23 and Fig. 24, where the critical bond strain for the horizon used here is 3×10^{-4}). To reach the location of these bonds (about 8 mm left of the impact center, and 2 mm above it), the P-wave takes about 1.42 μs from the MOI, the S-wave takes about 2.61 μs, and the R-wave arrives in about 2.84 μs. In Fig. 23, we see that critical strain is reached at around 3.15 μs after the MOI, leading us to conclude that the surface wave is the cause of initiating radial cracks on the top surface.

The surface wave forces nodes to move along the radial direction more than the other waves. The surface waves induce a close-to-elliptical motion for material points, and as the nodes move radially outward under this motion, the hoop strain increases. With this expansion, some of the hoop-direction bonds break, between nodes sitting on the same circle around the impact point. That is why the radial crack speed is not faster than the surface wave speed.

After the initiation phase, from about 7 to 15 μs from the MOI, the radial cracks propagation speed varies between a lower limit of about 1900 m/s and maximum values of about 2800 m/s, with an average around 2300 m/s (see Fig. 25). These values are for the velocity of the radial crack that initiates in the region highlighted in Fig. 22. Beyond 15 μs, waves reflected from the sides return and interact with the advancing radial cracks, slowing them down. Before 7 μs, there are many branching events near the impact zone, and it is hard to follow these cracks and determine their propagation speed. This average speed is significantly slower than the R-wave speed (see Sect. 2) and the question is "what sustains the radial crack propagation?" after them being initiated by the R-wave. Movie 9 shows how radial cracks form, and how they are left behind by the R-wave. We find that the propagation of the radial cracks is sustained by hoop pre-strain induced by the passing of the surface wave and the reinforcement provided by the shear waves bouncing through the thickness (TSS-waves). This is shown in what follows.

In Sect. 2 we specified the various wave speeds in glass. If the incident wave is an S-wave, then, Snell's law (Achenbach 1973) gives the following for the first critical angle θ_c:

$$\sin\theta_c = \frac{C_2^{\mathrm{PD}}}{C_1^{\mathrm{PD}}} \tag{2}$$

For our material model, this gives a value $\theta_c = 35.27°$. If the incident angle is smaller than θ_c, the reflection has both shear and longitudinal components. When the incident angle increases beyond the critical angle, the longitudinal component transitions into a surface wave (Achenbach 1973). To analyze possible connections between the radial crack propagation speed and the shear components reflected through plate's thickness, we calculate how fast these bouncing shear waves propagate in the specimen. The horizontal propagation velocity of the front of this train of TSS-waves (recall that we have spherical impact, not point impact) in the specimen is: $C_{\mathrm{horizontal}} = C_2^{\mathrm{PD}} \sin\theta_c \cong 1900$ m/s (see Fig. 26). This value is very close to the lower bound of the computed radial crack propagation speed. These waves appear to be the "engine" that sustains propagation of radial cracks. In the pre-strained environment induced by the passing of the surface wave, the radial cracks, that are initiated by the R-wave, start falling behind it. This slowdown is likely caused by the reduction in the

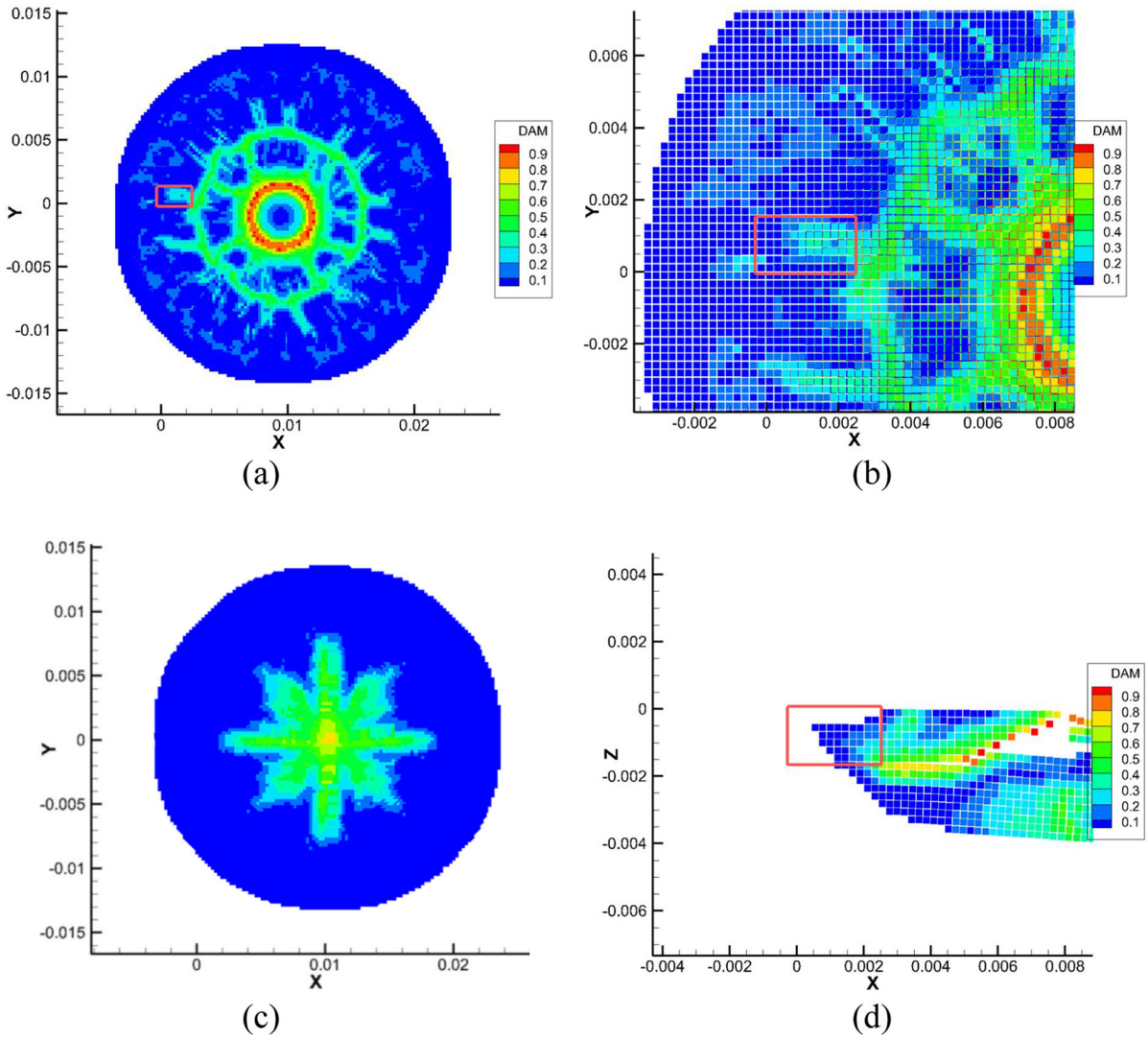

Fig. 22 Location of nodes taken from outside the second damage ring (which forms around 3.82 μs) used in Figs. 23, 24 and 25. **a**: top view of strike face; **b**: zoom-in around a radial crack to be investigated; **c**: bottom view of glass; **d**: cross section of glass plate around the region to be investigated. Undamaged nodes are blanked in these figures

amplitude of the R-wave: as the wave covers more area, its amplitude (in the in-plane direction) decreases and the hoop strains are not sufficient to break bonds at the same pace with its motion. The radial crack speed, however, does not fall below the "support" value of 1900 m/s. This appears to be because the TSS-waves reinforce the pre-strained material and "push" the radial cracks forward. This will be verified in the future by considering plates of different thickness and measuring the propagation speed of radial cracks, in both experiments and PD computations. This process continues as long as the waves amplitude are sufficiently high to induce bond failure. In our case, waves reflected from the boundaries of the sample return to interact with the advancing radial cracks at the end of the 7 to 15 μs period analyzed.

There are also radial cracks that appear between the first and second ring cracks (see Movie 2). They initiate after the formation of first and second damage bands. They are not caused by the surface wave because the hoop stress is partially released by the formation of the ring cracks. The TSS-waves, however, are slower than the TPP and TPS-waves that cause the ring cracks, so these radial cracks are

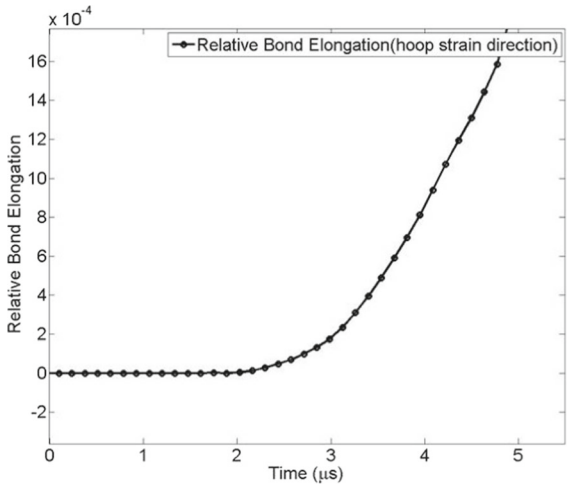

Fig. 23 Bond strain along hoop direction for a bond in the observation area in Fig. 22, which is normal to the radial crack direction and is cut by the radial crack

generated after the ring cracks. The bouncing shear wave through the plate thickness (the TSS-wave) is sufficiently strong this close to the impact location to induce critical hoop strains in the bonds in this region and lead to radial cracks (see Movies 2 and 5).

We can exclude the TSP-waves from the mechanism that sustains the propagation of radial cracks based on the much higher horizontal speed of these waves compared to that of the radial cracks. Figure 26 schematically shows amplitudes of nodal motion

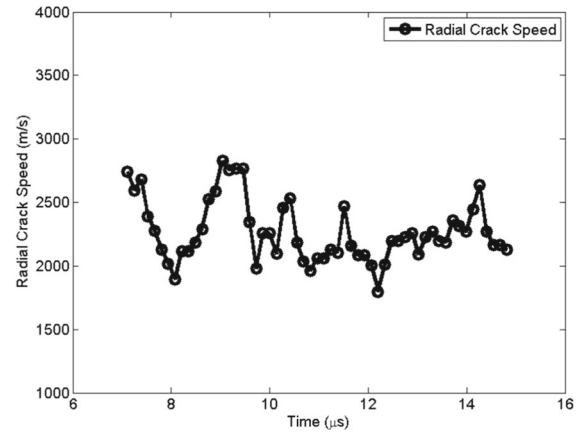

Fig. 25 The speed of radial cracks

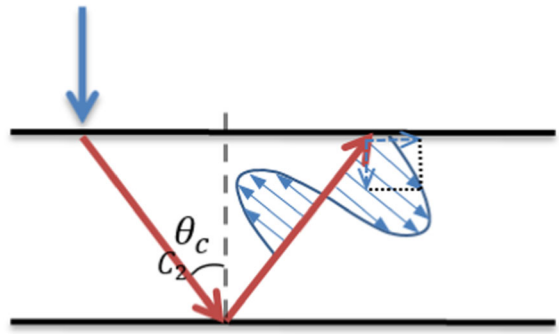

Fig. 26 The schematic of TSS-wave motion through the thickness of the glass plate

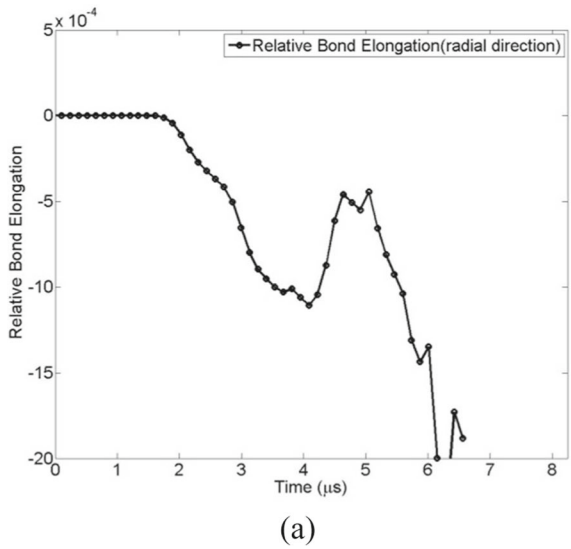

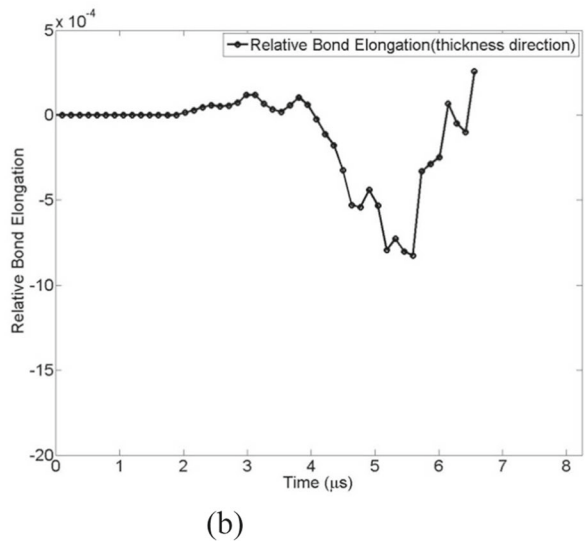

Fig. 24 **a** Bond strain along the radial direction (the P-wave direction); **b** Bond strain through the sample thickness direction. The nodes selected are in the observation area shown in Fig. 22

induced by the TSS-wave. The horizontal component of the motion caused by the TSS-waves pushes material away from the impact location, causing higher hoop strains. The pre-stressed material (due to the R-wave) fails as the reinforced motion leads to reaching of the critical bond strain for bonds aligned with the hoop direction. This appears to be the mechanism behind the propagation of radial cracks.

4.6 Cracks parallel to the sides of the plate

The formation of the sets of cracks that tend to align themselves with the boundaries of the square plate (see highlighted regions in Fig. 27) is described next. In the simulations, we capture parallel cracks, which will be named as follows: starting from the top of Fig. 27 or Fig. 28, moving clock-wise, E, F, G and H. Measured from the impact center, the peridynamic results show crack E's location to be 3.9 cm $\sim$ 4.0 cm away, crack F is 4.0 cm $\sim$ 4.5 cm away, crack G is -3.9 cm $\sim$ -4.1 cm away, and crack H is -3.5 cm $\sim$ -4.0 cm away. The locations of the parallel cracks from the experiment (see Fig. 27) are: crack E is 3.7 cm, crack F is 3.8 cm, crack G is -4.0 cm, and crack H is -3.2 cm, all measured from the impact location. The parallel cracks *location* is very close between the experiment and simulation. The tape used in the experiments on the sides of the two-plate system may absorb some of the incident stress waves. This could be the reason for which some of the parallel cracks in the experiment are not as pronounced as in the simulations.

We conduct a detailed analysis to understand the origin of the parallel cracks. We initially attributed, incorrectly, the origin of all such cracks to the reinforcement between the surface wave and the PS-wave. The detailed analysis below allows us to conclude that the picture is more complicated, and that other types of waves are involved in this process. To determine which particular wave interactions generate these cracks, we extract, from the simulations, the arrival times of different wave fronts at the locations where the parallel cracks initiate. Since the impact location is not at the center of the specimen, we observe that these parallel cracks are generated at different times (see Figs. 27 and 28) and different locations. In Fig. 28 we show the time snapshots of damage maps at which each parallel crack is first observed.

In Tables 1 and 2 we give the range of times needed for different wave fronts, incident and returning *directly* (shortest path) from the sides of the plate, to reach the closest and farthest of the damaged nodes at these locations, at the first time when damaged nodes show up around these areas. Because of the small thickness of the plate, the time of arrival of incident waves, wherever it hits the side of the plate, is about the same as the arrival time of a wave that moves

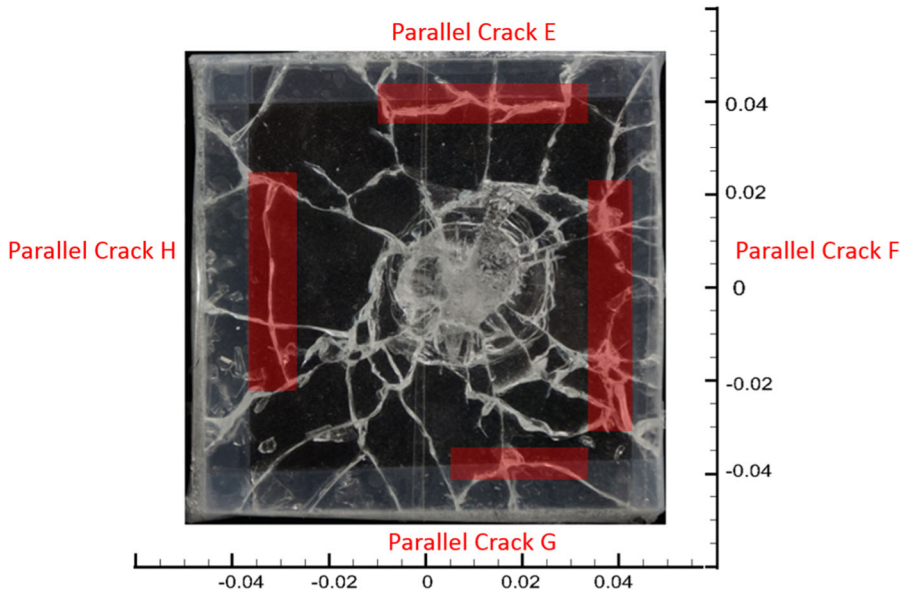

Fig. 27 The names and locations of cracks parallel to the sides of the plate (highlighted with red regions)

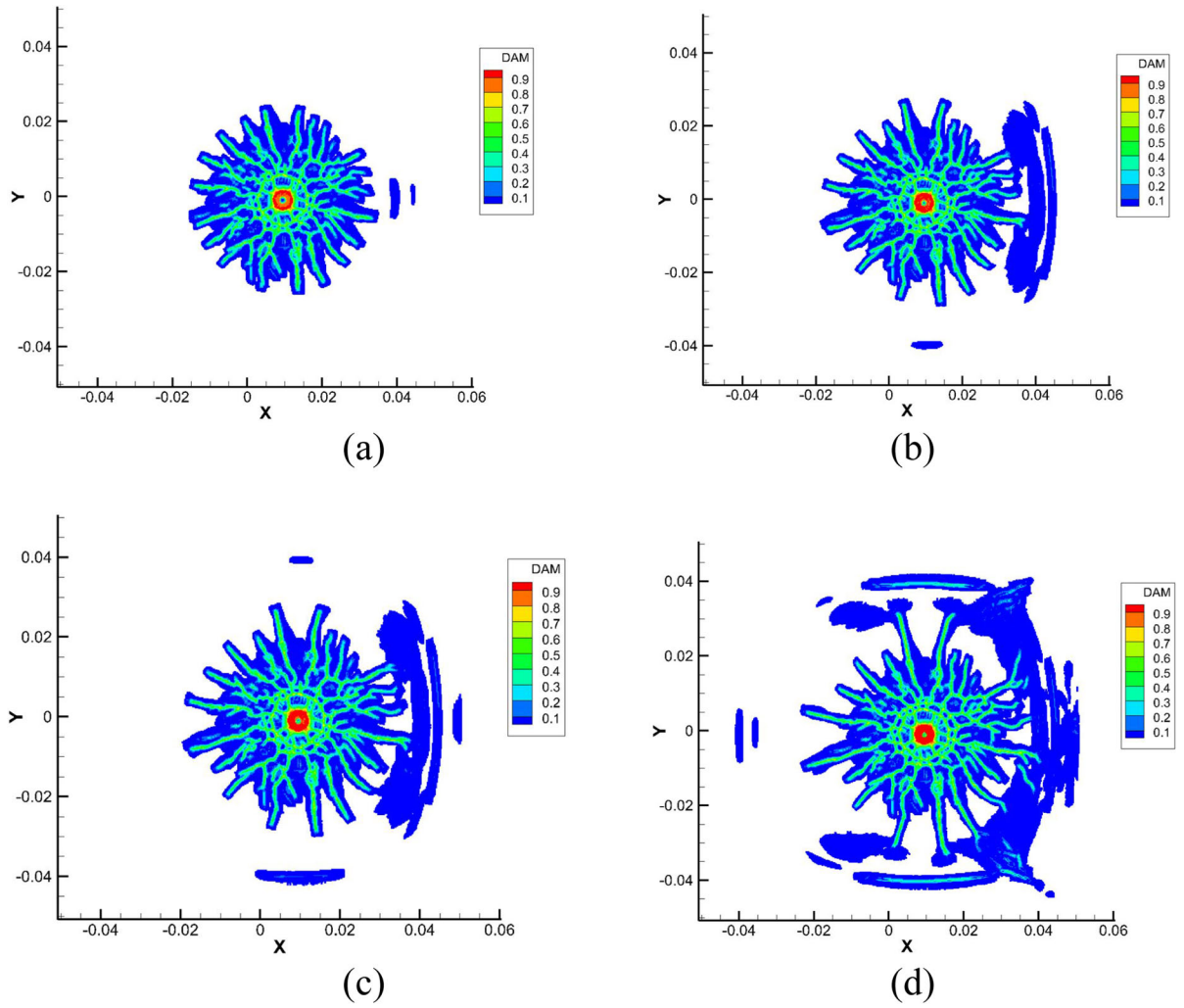

Fig. 28 Damage over the entire plate (blanking the undamaged nodes) viewed from the strike-direction: **a** crack F starts around 11.1 μs, **b** crack G appears at 12.75 μs, **c** crack E forms around 13.03 μs and **d** crack H starts around 15.5 μs

normal to the out-of-plane direction from the impact location to the sides. By analyzing the match between the times when the cracks form in the simulations, and the times at which different waves arrive at the locations where damage is observed (see data in Table 1 and Table 2), we find that many, but not all, of these cracks are generated by the interaction (reinforcement) between the PS-wave and the incident R-wave or the incident S-wave (coming from the impact region and moving towards the boundaries, see Fig. 28). Note that the PS-wave carries most of the energy of the reflection (Achenbach 1973).

Note that for crack systems E and G only one initiation point (on the top surface) is observed, while for cracks F and H there are two initiation points, one on the top surface and one on the bottom surface of the plate. The accuracy with which we determine the crack generation time is limited by the data output dumping frequency, and in this work this is $\pm 0.067\mu s$. To explain these differences, we next investigate similarities and differences between the formations of parallel cracks.

4.6.1 Crack G

Crack G starts in the computations at around 13.06 μs. Figure 29 gives the cross-section view of crack G, with color green showing any non-zero damage level

Table 1 Parallel cracks (E and G) generation times and times at which different waves arrive at the locations where damage is first observed

	Crack E (μs)	Crack G (μs)
Crack generation time	12.75	13.06
Incident S-wave	**12.24–12.55**	**12.15–12.54**
Incident Rayleigh wave (R-wave)	13.31–13.65	**12.76–13.45**
PS-wave	**12.48–12.79**	**11.89–12.50**
PR-wave	12.77–13.11	**12.16–12.82**
PP-wave	10.64–10.96	11.11–11.31

The waves likely to generate these cracks are highlight in bold

Table 2 Parallel cracks (F and H) generation times and times at which different waves arrive at the locations where damage is first observed

	Crack F (μs) (Damage on strike face)	Crack F (μs) (Damage on back face)	Crack H (μs) (Damage on strike face)	Crack H (μs) (Damage on back face)
Crack generation time	11.10	11.10	15.50	15.36
Incident S-wave	**10.54–10.79**	9.01–9.62	13.74–14.20	**14.98–15.59**
Incident R-wave on top face	11.47–11.74	**9.80–10.47**	**14.94–15.45**	16.28–16.95
PS-wave	9.14–9.39	**10.46–11.08**	**14.98–15.47**	13.75–14.37
PR-wave	9.23–9.57	**10.57–11.24**	**15.36–15.90**	13.89–14.56
PP-wave	8.36–8.50	9.12–9.49	13.28–13.54	12.49–12.85

Waves likely to generate these cracks are highlighted in **bold**, while those with a smaller likelihood are underlined

smaller than 0.9. To observe the wave interactions, in Fig. 30 we plot the out-of-plane nodal velocity components for the line of nodes which exhibit the initial damage in Fig. 29 (the 3rd layer from the strike face). We find that the out-of-plane motion is the likely cause for generating crack G.

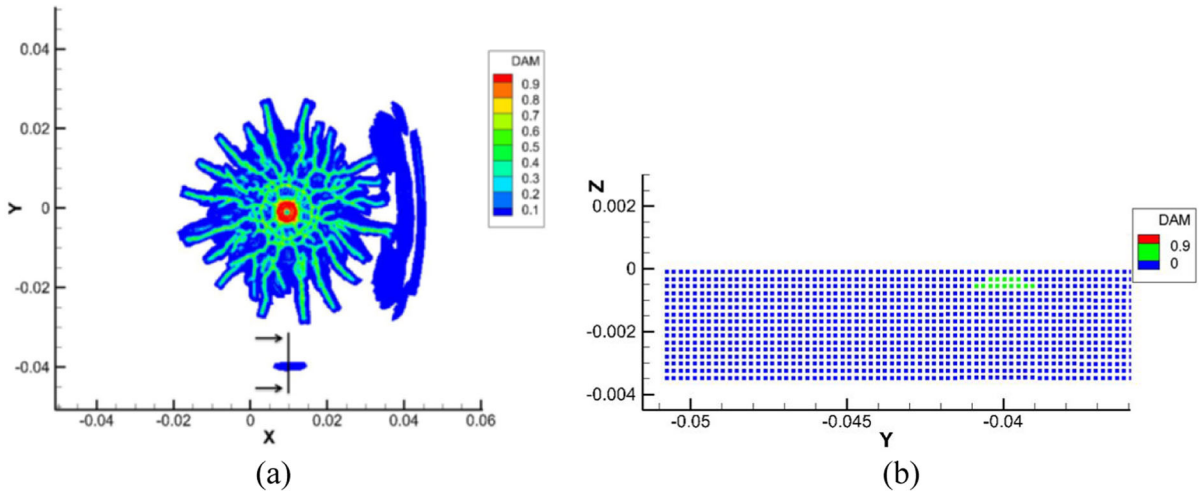

Fig. 29 Left: parallel crack G (damage plot as in Fig. 28, undamaged nodes are blanked); Right: damage map for through-thickness cross section near crack G, passing through the impact location

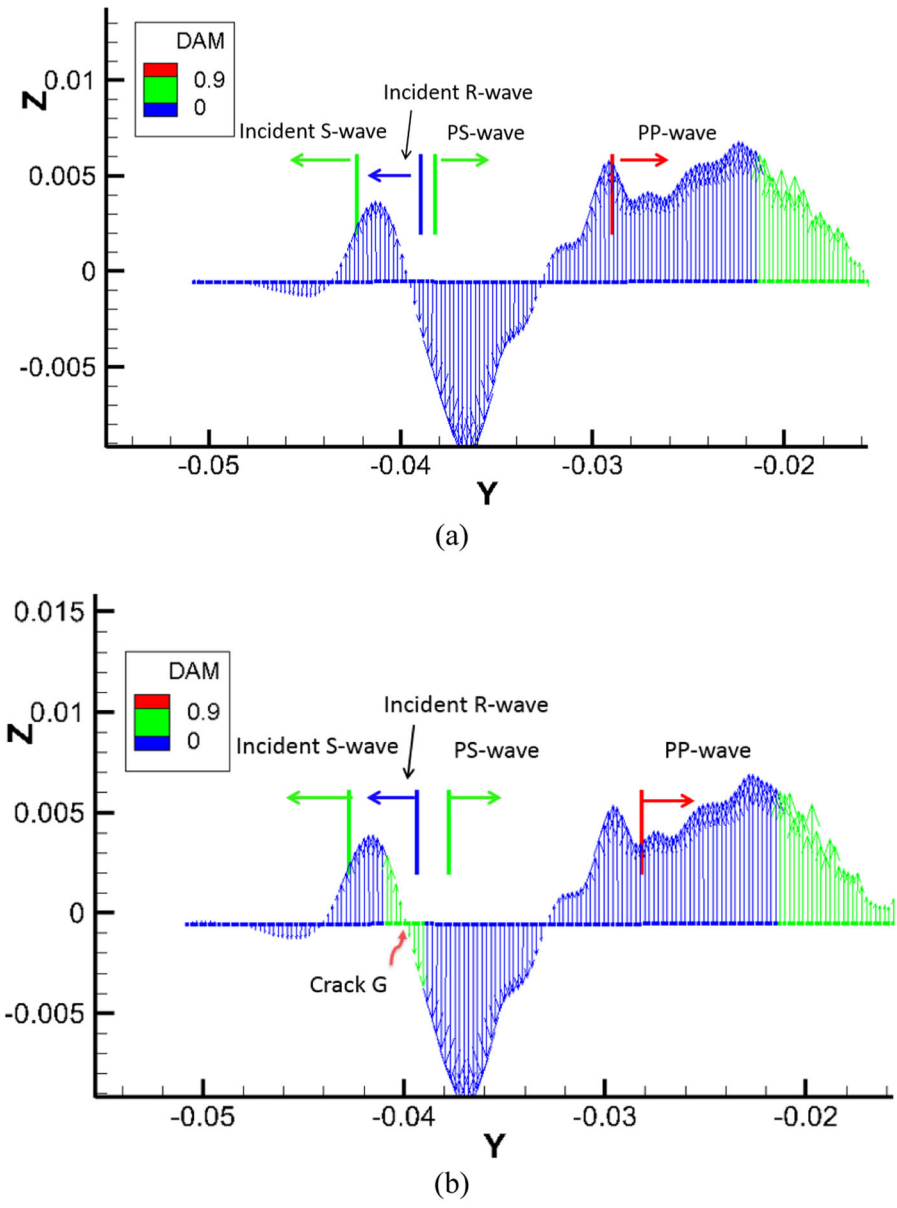

Fig. 30 Out-of-plane nodal velocity vectors for nodes in the 3rd layer from the strike surface (see nodes in Fig. 29) that cross crack G. The axes show the y- and z-coordinates of these nodes. Color of nodal velocity vectors represents nodal damage. In **a**: at 12.61 μs; in **b**: at 12.75 μs, showing the initiation of damage for crack G. The length of vertical arrows represents the nodal velocity magnitude of the nodes selected (the focus is on their rate of change, not their absolute values)

In Fig. 30, the color for the out-of-plane nodal velocity vectors represents the nodal damage state: blue means no damage, green is any damage level less than 90%. The two snapshots given in this figure point to the time of initiation of crack G, between 12.61 μs and 12.75 μs after the MOI. The vertical bars accompanied by horizontal arrows show the arrival locations for the different stress wave fronts. Their color is not connected to the color bar used for the nodal damage. The horizontal arrows indicate the direction in which a particular wave is moving at that moment. From Table 1, at the times used in Fig. 30, only the PS-wave and the S-wave both just passed the initiation location of crack G. The PR-wave is right behind the PS-wave. The time gap between the PR-wave and crack G initiation time is smaller than that for the PS-wave, leading us to conclude that crack G may be generated by the PR-wave reinforcing the S-wave. Notice also that the incident surface wave on the strike surface has not yet reached the crack location when crack G initiates. Similarly, the PP-wave has already passed

the crack location without damaging the material, at this time.

We notice that the moment the two wave fronts (S and PR, for example) meet, the parallel crack is not initiated right away. The maximum strain induced in a bond does not happen when the wave fronts reach the corresponding location, but shortly after that, when the intersecting waves induce peak rates of change of the magnitudes of the out-of-plane velocity component, resulting in bonds being strained beyond the critical strain (see Fig. 30). This deformation mechanism stretches bonds the most, and that is when the crack is generated (see Movie 10). In Movie 10 we monitor in time the line of nodes shown in Fig. 30, and use the moving markers (vertical bars) to keep track of the fronts of various elastic waves and their reflections from the plate's edge.

4.6.2 *Crack E*

The impact location is almost symmetric about the x-axis, and because of this, Crack E is similar with Crack G: the incident shear and the shear-component of the reflected longitudinal wave generates this crack. For this case, however, the edge of the glass is a little further from the impact center than in Crack G case (due to asymmetric impact), therefore the reflected wave propagates over a longer distance, and the separation between different reflected waves grows slightly.

The data in Table 1 shows that the crack initiates soon after the two waves, incident S-wave and PS-wave, reinforce each other. Movie 11 shows the out-of-plane nodal velocity for nodes in the 3rd layer from the strike surface (see Fig. 31) and explains the waves interactions responsible for initiating Crack E. The moving markers in Movie 11 track the fronts of the various elastic waves and their reflection from the top edge of the plate in Figs. 27 and 31.

4.6.3 *Crack F*

A little different from parallel cracks E and G, the parallel crack system F starts on the 2nd and 3rd layers from the back face (see Fig. 32) *and* on the 3rd layer from the strike face, at about the same time.

The spatial rate-of-change of the nodal out-of-plane velocity vectors can be seen from plots in Fig. 33. Damage correlates with the locations where these rates of change are largest, since, as discussed before. For crack system F, the initial damage appears almost at the same time near the strike and back surfaces, for the dumping frequency used here. It is likely that damage on the back surface appears first, because there are already two layers of damaged nodes for that location in Fig. 32. The plots in Fig. 33 indicate that the reinforcement between PS or PR-wave with the incident Rayleigh wave traveling on the back face (which is about 0.8 μs behind the one shown in Fig. 33 and tracked in Table 2) is the likely cause for generating the damage near the back surface. The data in Table 2 supports this conclusion. Movie 12 shows

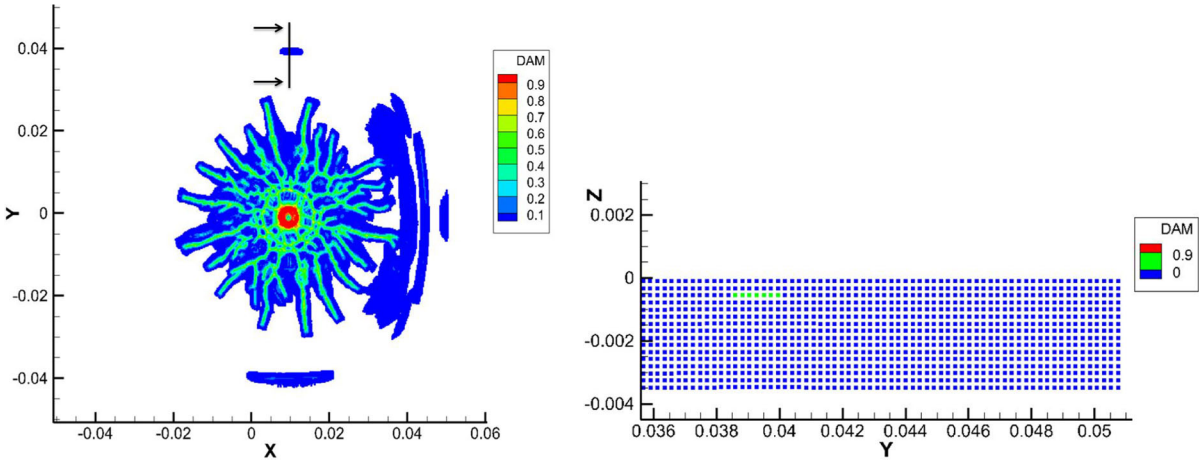

Fig. 31 Left: Crack E generated at 13.16 μs (damage plot as in Fig. 28), Right: damage map for through-thickness cross section near crack E location, through the impact point

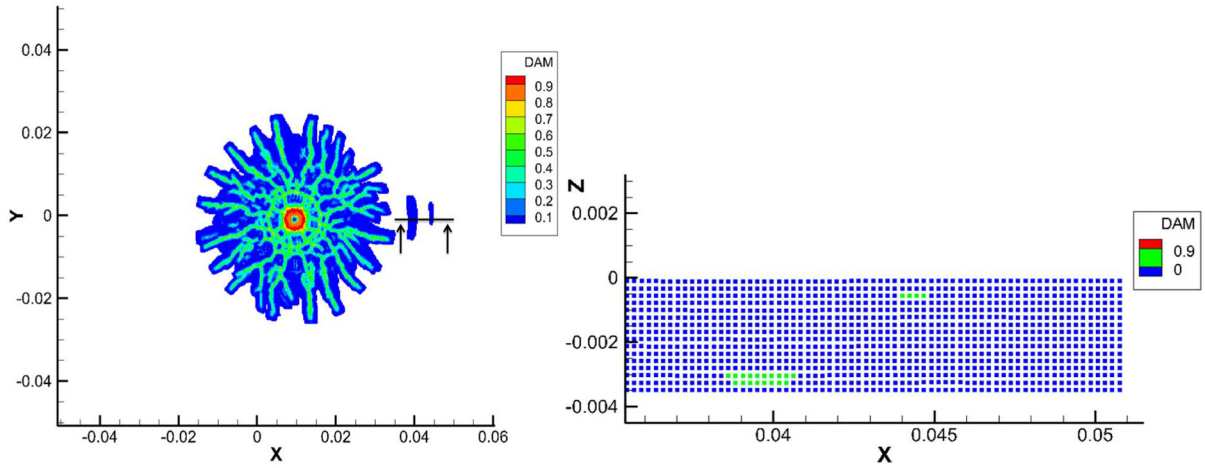

Fig. 32 Left: crack system F generated at locations shown at 11.1 μs (damage plot as in Fig. 28), Right: damage map for through-thickness cross section near crack F location, through the impact point location

the waves initiating Crack F. The damage near the strike face, however, does not seem to have been generated by the incident waves reinforcement with the PS-wave, since the PS-wave has long passed the location of where the damage is. A possible explanation for occurrence of this damage can be based on the arguments used to explain the driving force behind the sustained growth of radial cracks in Sect. 4.5, namely TSS-waves produced by the PS-wave. The working hypothesis is that the longitudinal wave reflecting from the edge of the plate produces shear wave components that, besides moving straight back towards the impact zone, they bounce between the strike and back plate surfaces. This creates a delayed arrival of this shear wave, which, we assume, meets now with the S- and R-waves and reinforces them, causing damage. Verification of this hypothesis requires further investigation, which we plan to do in the future.

An explanation is now needed for why the interaction that caused crack systems E and G, happens only on the back face for the F crack, and not on the top face. The likely reason for this behavior is the impact type. While simple arguments can be used about traveling waves into the plate for the case of point-loading, our case with a spherical rigid-body impact is more complicated: trains of waves are induced into the plate and their complex reflections from the plate's side boundaries lead to wave reinforcements that are not uniform in time and space and, therefore, depend on the distance from the impact point to the reflecting boundary. A partial verification of this hypothesis is in the next section.

We also remark that this through-thickness crack is tilted, not cutting straight, because its top and bottom initiation points do not have the same x-coordinates. This type of behavior is seen in the experiment as well, with many of the through-thickness cracks showing a twisted surface instead of the flat one, as can be seen from Fig. 4.

4.6.4 Crack H

For crack H, the initial damage is also generated in two different regions almost at the same time, near the strike and back surfaces of the glass plate. However, compared to what happened for crack F, damage near the back surface is closer to the edge of the plate, while for F it was closer to the impact center. To answer this puzzle, we observe that the first damage initiation near the back face happens at around 15.36 μs. At 15.5 μs, damage near the strike surface is initiated as well (see Fig. 34). The cause for damage on the back face cannot be the reinforcement of S-wave with PS-wave or PR-wave, since PS-wave and PR-wave, by the time damage forms at this location, have already passed by (Fig. 35). Therefore, the other hypothesis, mentioned in the previous section, is as follows: the reinforcement between the S-wave and a TSS-wave produced by the PS-wave. Why then the mechanism that created cracks E and G does not cause a crack in this case?

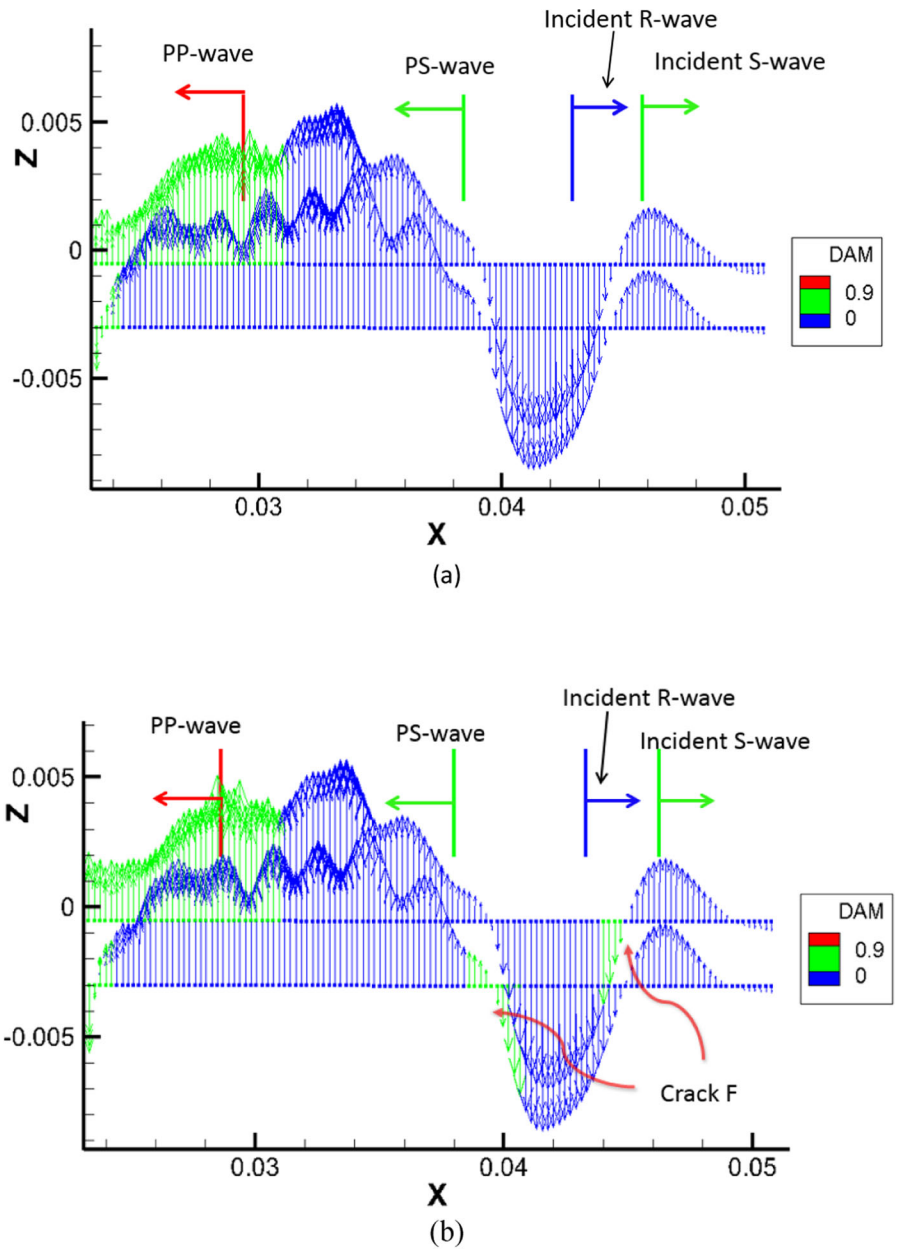

Fig. 33 Out-of-plane nodal velocity vectors for nodes (crossing crack F) in the 3rd layer of nodes below the strike glass surface and the 3rd layer above the back side of glass plate. **a** 10.96 μs; and **b** 11.10 μs from MOI. **b** captures initiation of damage for crack F

This is probably because the side boundary for crack system H is the farthest away from the impact center, therefore, the PS-wave and PR-wave that reflect straight from the boundary have lower amplitudes. However, subsequent bouncing of the PS-waves between the strike and back faces (the TPSS-waves, part of the Lamb waves) may be able to create sufficient reinforcement for out-of-plane motion that the interaction with the S-wave causes local damage.

The answer for the puzzle with crack systems F and H (the flip between the cause of damage between the strike face and the back face) is as follows: the spherical rigid-body impact induces complex reflections from the plate's side boundaries that lead to non-uniform wave reinforcements that depend on the

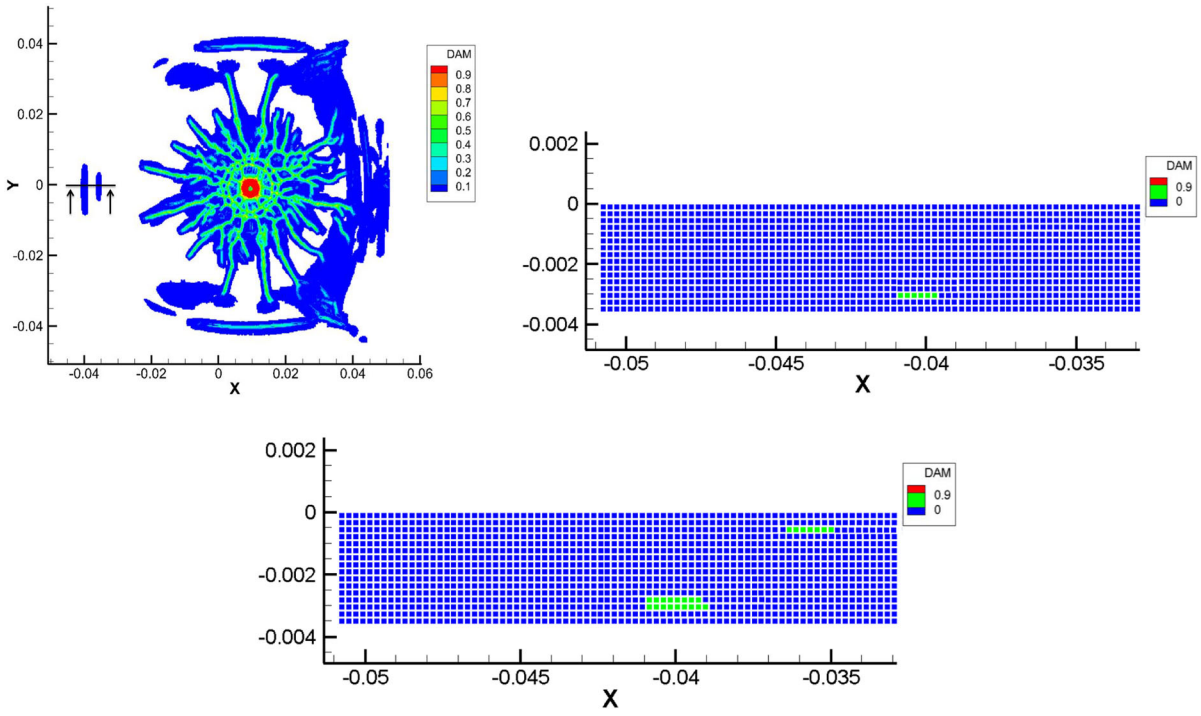

Fig. 34 Top Left: crack system H generated at locations shown at 15.5 μs (damage plot as in Fig. 28); Top Right: damage map for through-thickness cross section near crack H, through the impact point location at 15.36 μs; Bottom: same cross-section at 15.5 μs

distance from the impact point to the reflecting boundary. The asymmetric impact we used leads to different distances to the side boundaries, which, combined with the train waves complex reflections, are responsible for the different damage mechanisms of the crack systems parallel to the plate edges.

The cause for damage on the strike face is, likely, the interaction between PS- and R-waves, since the arrival times match the crack generation time (see Table 2). Movie 13 shows the waves initiating Crack H.

4.6.5 Discussion and summary

In summary, we can conclude that parallel cracks were generated by an incident out-of-plane wave enhanced by a reflected out-of-plane wave. In Table 3, we summarize the reinforcements of waves that appear to be causing the cracks parallel to the sides of the plate. The differences noticed between the initiation times, locations, and types of cracks (only near the strike face or both near strike and back face) for these crack systems are likely due to differences between matching of the phases of the interacting reflected waves and incident wave.

4.7 Edge-to-Center (E2C) cracks

The experiments appear to show (see Fig. 1, especially close to the right boundary) that some radial cracks split/branch as they approach the boundaries. The simulation results for damage at 99 μs after MOI shown in Fig. 5 indicate the presence of such crack branching events (see near the right boundary). The computations show, however, that some of these branching events are in fact the coalescence of two types of cracks, not the splitting of a single crack, at its tip, into two or more branches. This can be seen from Movie 2 and from Fig. 36. Some cracks appear to initiate on the boundaries of the sample and grow towards the center (we will refer to these "edge-to-center" cracks as E2C cracks). As shown in Fig. 36, a radial crack twists as it propagates towards the edge (due to interactions with waves and the parallel crack) and it meets an E2C crack, making the final damage pattern look like as if a single crack split into two branches. Movie 14, using a similar viewpoint to Movie 2 but only showing nodes that have a damage index higher than 0.1 (allowing a 3D view of damage evolution), demonstrates that crack patterns which, post-mortem, look like branched cracks, can have two

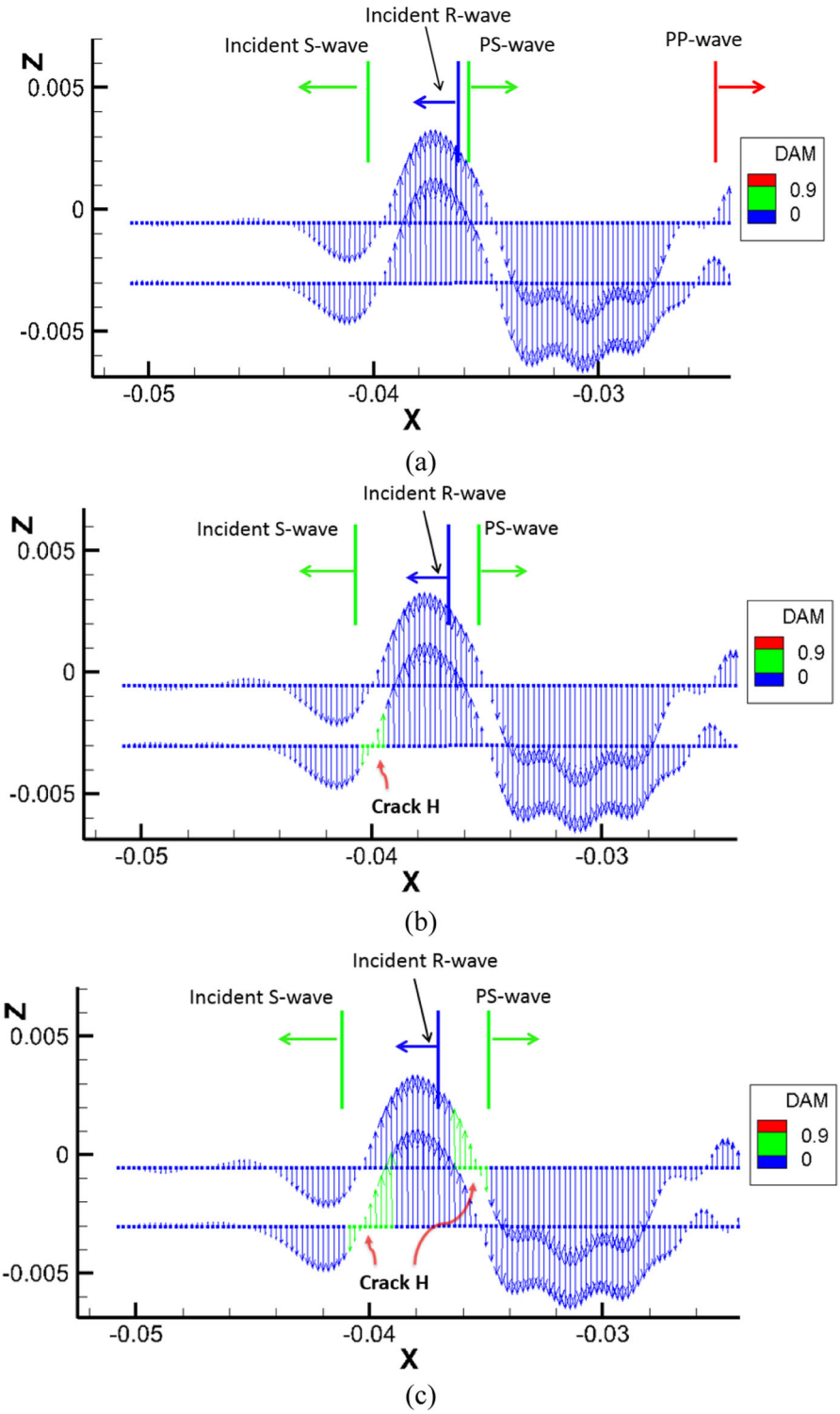

Fig. 35 The out-of-plane nodal velocity vectors for nodes (crossing crack H) in the 3rd layer below the top surface and 3rd layer above bottom surface of glass. **a**: at 15.23 μs; **b** at 15.32 μs; and **c** at 15.50 μs, after MOI. **b** and **c** show initiation of damage for crack H

Table 3 Possible wave reinforcements that cause the parallel crack systems

		Wave reinforcements causing cracks parallel to the sides of the plate
Crack E		Incident S-wave & PS-wave
Crack F	Second (and closer to the edge): damage on strike face	Incident S-wave & TPSS-wave
	First: damage on back face	Incident R-wave & PS-wave
Crack G		Incident S-wave & PS-wave (or PR-wave)
Crack H	Second: damage on strike face	Incident R-wave & PS-wave
	First (and closer to the edge): damage on back face	Incident S-wave & TPSS-wave

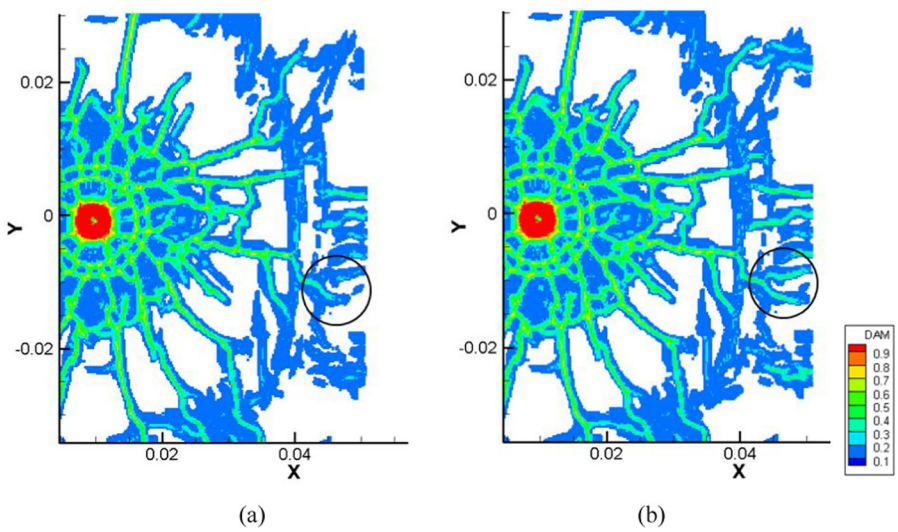

Fig. 36 Crack coalescence between a radial crack with an edge-to-center crack, leading to apparent crack branching (damage plot as in Fig. 28, but blanking nodes with damage below 10%)

origins. The first is a true crack branching event, in which radial cracks at high propagation speed and interacting with stress waves split, at their tip, into two branches (see Bobaru and Zhang 2015; Ha and Bobaru 2011b), and a second one, which we call "fake branching", that results from the merger of a crack with an existing crack path. The fake branching, in which the two cracks generally run in opposite directions, can happen even at low crack growth velocities. At such crack propagation speeds, stress waves can easily induce significant tortuosity in the crack paths.

To investigate whether E2C cracks happen in reality, we analyze the post-mortem fragments. Fractography results show that there are some cracks (closest to the corners of the plate) that indeed move E2C. Glass fragments were dissembled from the specimen to determine the direction of crack propagation. The fracture surfaces of the cracks were examined using techniques described in both the American Society of Standards and Technology (American Society of Testing and Materials) standard ASTM- C1322-15 (ASTM 2019) and in Quinn (2006). The specimens examined optically using a dual station WILD microscope. Regions of interest R1 and R2 can be seen in Fig. 37 with the directions of cracks labeled P_1 to P_5, and Q_1 to Q_3, and propagation direction marked. These regions were selected because of the high number of cracks predicted by the model to have originated from the outer edge, running towards the center.

Of the eight cracks studied, cracks P_5 and Q_3 (see Fig. 38) were observed to originate at or near the specimen edge and propagate from the edge to the center (E2C) with the remaining cracks propagating center to edge. On crack P_5, the observed placement of the Wallner lines as well as twist hackle propagating towards the back face indicate that the crack initially

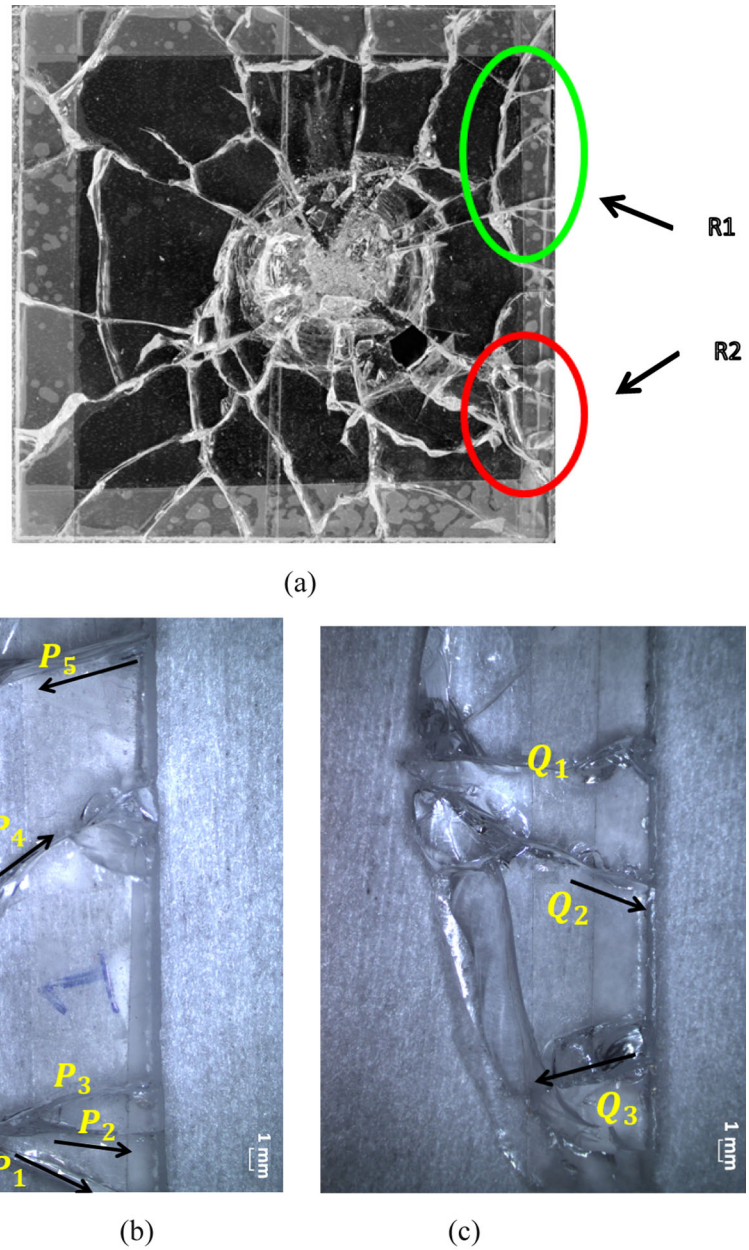

Fig. 37 **a** Back-face view of the glass plate. Tape was used in experiments along the sides to keep the glass plate together with the PC backing plate so that the fragments can be collected post-mortem. The PC plate is removed in the photo. **b** Region R1 and **c** Region R2 with crack propagation directions marked as determined by fractography

propagated with a leading edge on the strike face and broke through to the back face later. This would be indicative of a bending condition where tension existed on the strike face, and compression existed on the back face. Such conditions could be promoted by wave reflections from the edge of the sample and by the presence of the tape, holding the glass plate and the PC backing plate together on their edges. No clear fracture origin was identified for crack P_5. Crack Q_3 originated from a chip located on the edge of the back face and propagated toward the center of the specimen. The twist hackle observed on the fracture surface (see Fig. 38) indicates a complex multiaxial stress state causing a twisting motion as the crack propagated. It is likely that the complex stress state was induced by the reflected shear waves bouncing through the thickness of the plate (TPSS-type waves, a Lamb-type wave, see Fig. 6 and Sect. 4.6).

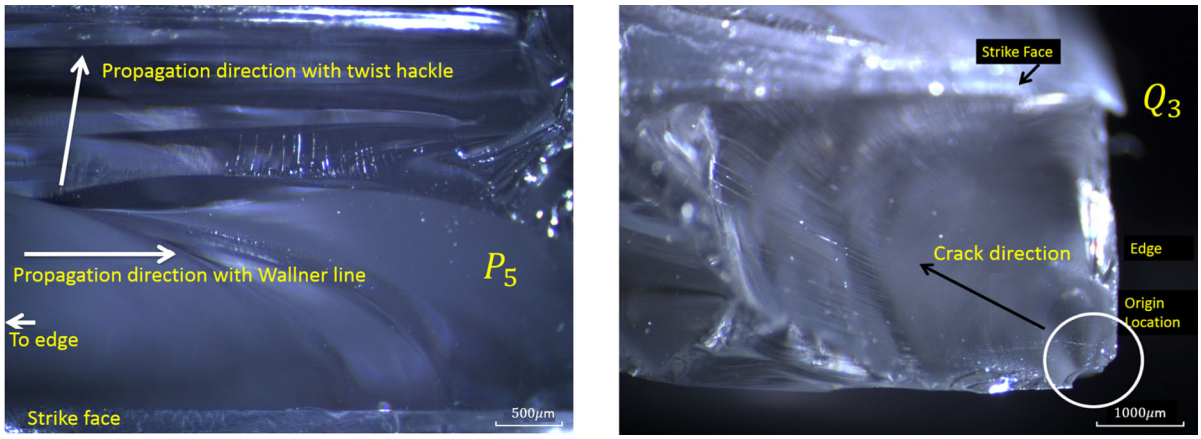

Fig. 38 Optical microscope images of fracture surface for cracks P_5 and Q_3 shown in Fig. 37

Next, we explain how the E2C cracks are generated in the simulation results, and discuss wave interactions that drive their growth.

In Fig. 39, highlighted by the red circles, the 1st sets of E2C cracks appear at around 12.9 μs, 16.74 μs, 17.29 μs and 23.61 μs from the MOI, respectively, for the right, bottom, top and left sides of the plate. The first S-waves starting at the impact point reach the right, bottom, top, and left boundaries in Fig. 39 at 12.64 μs, 15.38 μs, 15.94 μs and 18.76 μs after MOI, respectively. For the first incident R-wave these numbers would, correspondingly, be 13.75 μs, 16.85 μs, 17.34 μs, 20.30 μs.

In Fig. 40 we show the upper right quarter of the specimen and plot the out-of-plane nodal velocities with their actual magnitudes and the colors indicate the damage index shown in the figure legend. For this plot, we select only the first layer of nodes on the strike-face and tilt the figure slightly to better see the out-of-plane velocity vectors (see Fig. 40). The figure shows that when a wave front reflects from the boundary and interacts with the train of incident waves (caused by the sphere impact), damage occurs near/on the edge (see the black-line highlighting the front of the wave front). When the first wave front "splashes" on the side and "folds-back", tensile stresses develop that lead to mode I cracks advancing from the edge towards the center.

The "folding" of the first wave front caused by the reflection from the side surface continues to propagate along the boundary towards the corners of the plate, and, as it does so, continues to meet and reinforce the next incident wave front. When the reinforcement between these two waves reaches critical values, damage develops (see Fig. 40c). Once the strain energy is locally released by the breaking of bonds, the traveling reinforcement reduces and can produce new damage only when it builds up again, as can be seen from Movie 15 and from comparing the results in Fig. 40b, c, f (see highlighted damage regions with yellow ellipses). This explains the existence of a particular spacing between such cracks.

The simulation results also indicates that the second and third damage regions that initiate near the boundary (see damage highlighted in Fig. 40c and f) is produced slightly inside the sample, corresponding with a location of maximum bond strain due to wave reinforcement. The fractographic analysis indicates that crack Q3 initiated at a chip on the edge of the specimen. It is possible that the near-edge damage associated with this chip is co-incident with the maximum bond-strain region predicted in the model.

Recall that fractography results showed that only the edge cracks nearest to the corners of the plate had E2C growth (see Fig. 37). In the simulations, all cracks that grow from the edge or near-edge regions appear to advance E2C. Why this difference? We believe that this difference can be explained by the presence of the tape in the experiment, and its absence from the simulations. The tape absorbs and transmits a portion of the energy to the backing plate, which likely reduces the chance of fracture near the plate's edge. Eventually, radial cracks in the experiment move in and reach the edges of the plate. This is the case for cracks P_1, P_2, P_4, Q_2. On the other hand, the cracks computed by PD that correspond to P_5 and Q_3, are

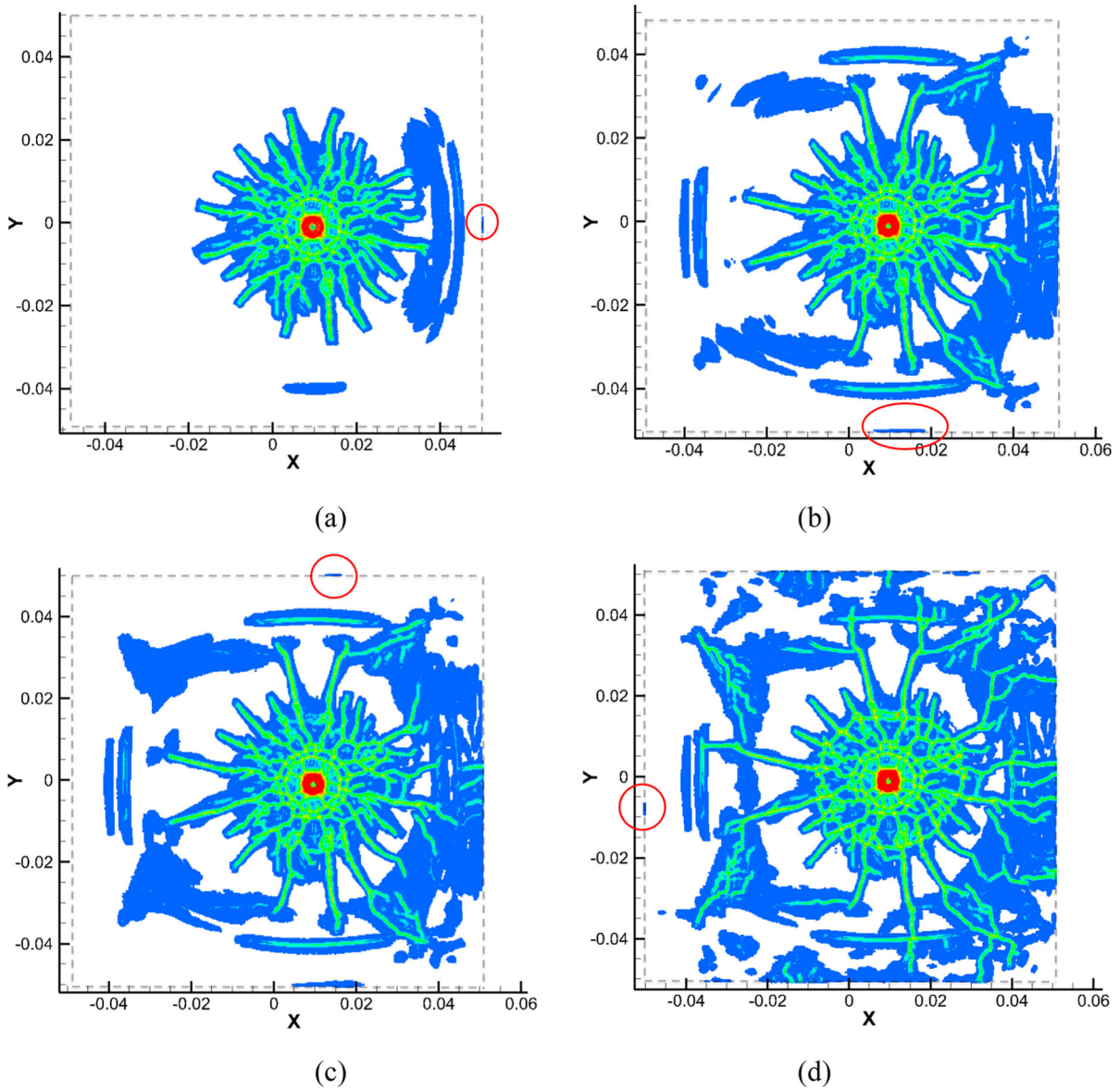

Fig. 39 Initiation of damage on the sides of the plate (damage index legend as in Fig. 28 but blanking nodes with damage below 10%; gray dashed-line shows the edge of the glass plate) at 12.89 μs, 16.74 μs, 17.29 μs and 23.61 μs from MOI

shown to initiate slightly further away from the edge of the plate (see Fig. 41). If that is the case in the experiment as well, then the presence of tape has less influence on initiation of damage at these locations, closer to the corners of the plate. Note that the simulation results for the bottom right quadrant of the plate show a similar behavior to that of the top right quadrant discussed above (see Fig. 42 and Movie 16).

We observe that for cracks with the same growth direction between the experiments and the simulations, their locations (see Fig. 43) match very well (see red circle highlights in Fig. 43).[2]

[2] The strong influence of boundary conditions in brittle fracture should not be surprising. A famous example is the failure of the Tesla Cybertruck "unbreakable" windows after they were struck with a metal ball. The failure was not supposed to happen, but prior to the public test, the door was apparently hit with a sledgehammer, which likely changed the boundary conditions on the glass, if not fractured it at its base.

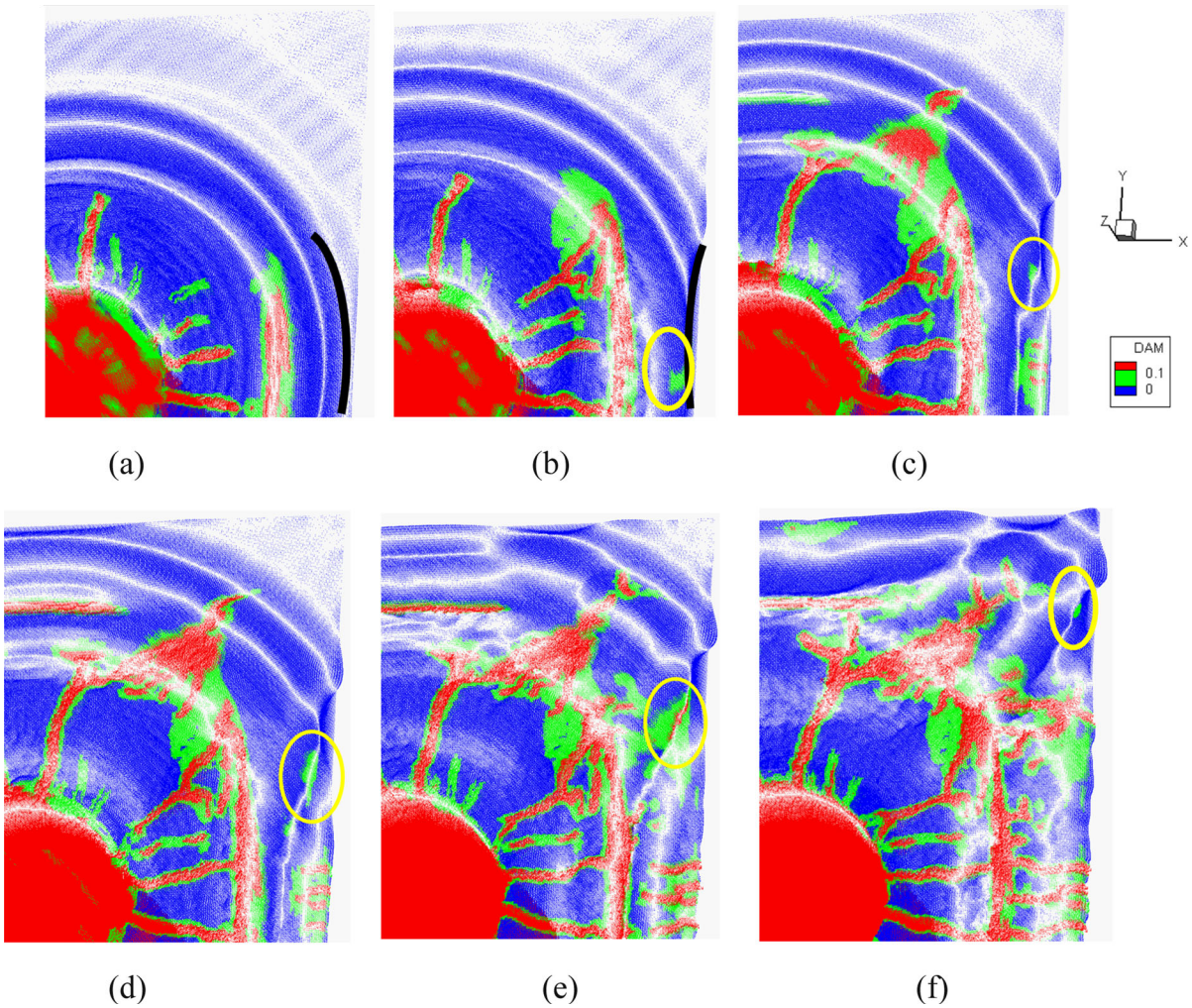

Fig. 40 Evolution of edge-to-center cracks on the top-right quadrant of the glass plate. Titled view of the out-of-plane component of the nodal velocity (magnitude proportional to the size of the arrows) and damage index D (blue: D = 0, green: $0 < D < 0.1$, red: $0.1 \leq D \leq 1$) only for the nodes on the strike surface of glass plate. Snapshots taken at 11.93 μs, 13.85 μs, 14.95 μs, 15.64 μs, 17.15 μs, 19.49 μs after impact. Notice (in the yellow elliptical shape) the damage generated by wave reinforcement

5 Conclusions

A simple peridynamic model, in conjunction with experiments, allowed us to explain the evolution of fracture and damage in a thin glass plate, backed by a thin polycarbonate plate, under impact. We studied damage progression from impact with a small projectile hitting at 150 m/s. A linear-elastic and brittle fracture model appears to be sufficient for explaining the entire complexity of fracture evolution in this impact event. The input parameters are, likely, the minimal set possible for modeling this phenomenon. No special crack propagation criteria were needed. All of the experimentally observed features of damage and fracture systems, obtained from post-mortem analysis of the sample and fractography studies, are replicated by the peridynamic simulations. We analyzed the simulation results to explain the reasons behind the formation of the different sets of cracks and the possible mechanisms responsible for the experimentally-observed evolution of damage in the glass plate. A number of 16 simulation movies accompany the paper and help support the explanations provided.

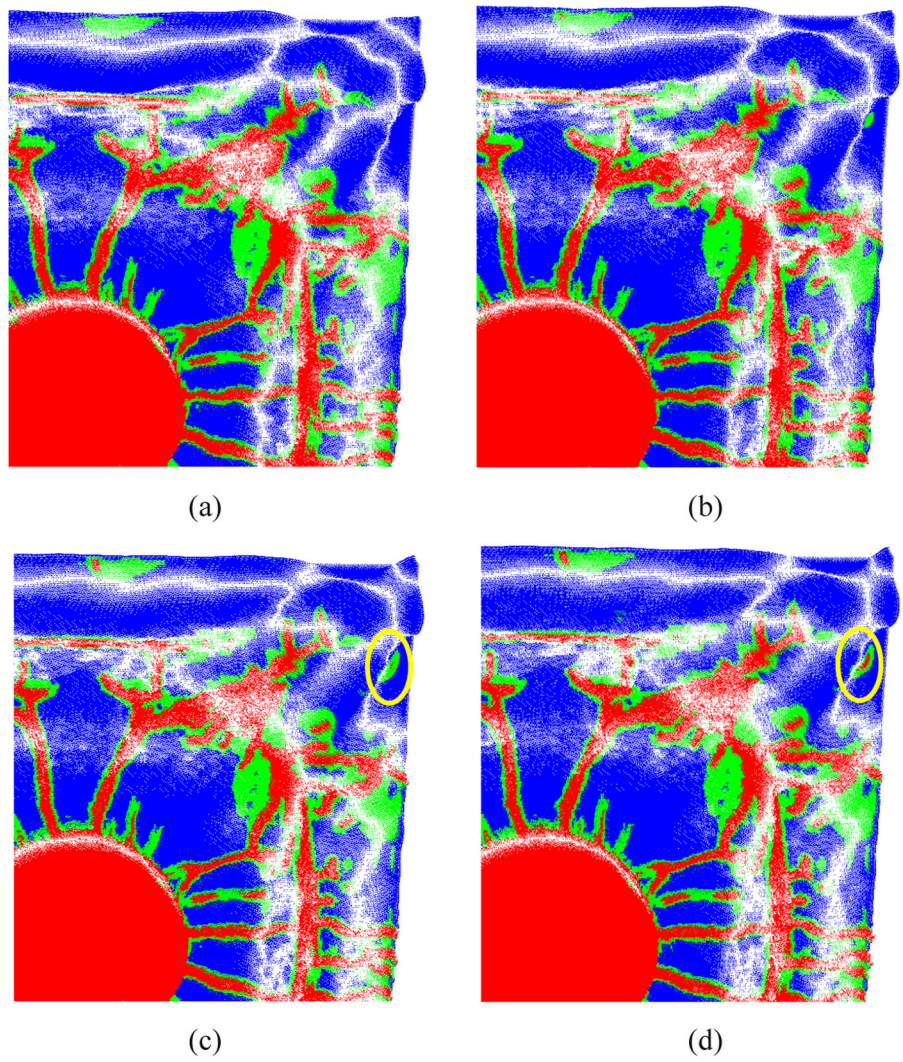

Fig. 41 Plots as in Fig. 40, for snapshots taken at 19.21 μs, 19.49 μs, 19.76 μs and 20.31 μs after impact. Notice (in the yellow elliptical shape) the damage generated by wave reinforcement

The peridynamic results for the band (or ring) cracks, that form soon after impact, match the expected results from analytical calculations based on wave propagation and through-thickness reflections. The Hertz-cone crack and fragmentation in the Hertz-cone areas are very similar to the type and size of fragments seen in the post-mortem analysis of the sample. Among all different types of cracks, one particular detail of the failure process in the glass plate is especially interesting and is captured by the, relatively coarse, peridynamic simulation: the fine roughness on the surface glass chips produced at the ends of the Hertzian-cone crack, when this crack turns and grows close-to-parallel to the strike face. The peridynamic simulations show that this roughness happens at low crack propagation speed and that it is caused by waves (Lamb waves) reflected from the side surfaces of the plate, hitting against the leading edge of the slowly-propagating Hertz-cone crack.

We explained the generation of radial cracks, and discussed the waves (Lamb waves) that sustain their propagation at speeds above a certain threshold which is significantly lower than the surface wave speed. We provided explanations for how cracks parallel to the sides of the plate are produced. Factors that are responsible for these cracks are reinforcements between incident shear and/or surface waves with shear components of the reflected (from the side surface) longitudinal wave, that may also bounce between the strike and back faces of the glass plate

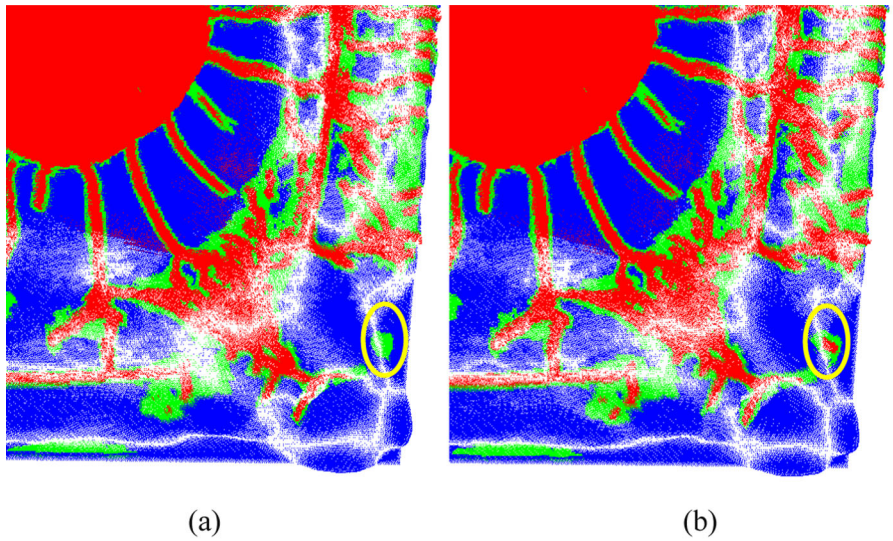

Fig. 42 Evolution of edge-to-center cracks on the bottom-right quadrant of the plate (snapshots at 19.35 μs and 19.63 μs after impact). Plots as in Fig. 40. Notice (in the yellow elliptical shape) the damage generated by wave reinforcement

(Lamb waves). The simulations showed some cracks growing from the edges towards the impact center, and fractography analysis confirms this behavior for those closest to the corners of the plate. The presence of tape on the sides of the plates in the experiments may explain the difference between the simulations and experiments for the rest of the edge-to-center cracks. We discover that a "folding" shear-wave reflected by the side surface of the plate reinforces incident shear/Lamb/surface waves and leads to initiation and propagation of these cracks with a specific spacing between them.

Peridynamic models are useful in investigating damage evolution in brittle materials, where interactions between stress waves and crack initiation, growth, and coalescence play a crucial role. This study explained the "how?" and "why?" damage progression happens in brittle materials like glass under impact. This can be very helpful in predicting impact damage in a variety of applications, such as designing better protective systems, controlling damage evolution in brittle materials, etc.

Acknowledgements Y.W and F.B. acknowledge the support from the AFOSR MURI Center for Material Failure Prediction Through Peridynamics (program managers Dr. James Fillerup, Dr. Ali Sayir, Dr. David Stargel, and Dr. Fariba Fahroo), from the ARO (Grant Number W911NF1010431, program manager Dr. Larry Russell), and from the ONR Award #N00014-16-1-2173 (program manager William Nickerson). F.B. was also supported by the NSF CMMI award #1953346. We thank Shumin Li (UNL) for performing the laser scan shown in Fig. 19.

Author Contribution F.B. procured research funding, coordinated the investigation, designed the computational investigation, and wrote the manuscript. Y.W. designed and implemented algorithms, conducted the numerical tests, created the plots and simulation movies, obtained data shown in tables, and wrote the manuscript. C.F.Y., J. Y., and J.W. designed, performed, and wrote the experimental part of the manuscript. All authors reviewed the manuscript.

Data availability No datasets were generated or analysed during the current study.

Declarations

Conflict of Interest The authors declare no competing interests.

Appendix A

Convergence tests in terms of damage patterns

Here we test several PD horizon sizes in a δ-convergence study (see Bobaru et al. 2009; Chen and Bobaru 2015) and analyze their effect on the general appearance of damage (see Bobaru and Zhang 2015).

As discussed in Sects. 2 and 3, the effective elastic wave speeds in this PD model for glass are: $C_1 = 5632$ m/s for longitudinal waves, $C_2 = 3252$ m/s for shear waves, and $C_R = 2990$ m/s for Rayleigh wave speed. The values for C_1 and C_2 were obtained by using the computational results for the impact test to measure the speed of the longitudinal wave front (tracked by

the nodes with non-zero velocity) and the in-plane shear wave front (tracked by the nodes at which there is angle change in the in-plane velocity vector). The value for C_R was computed using the formula in Eq. (1). These values are roughly within 5% from the corresponding values in soda-lime glass. While a state-based PD model (see Silling et al. 2007) would be able to exactly match all of the elastic constants in the materials used here, the computational cost compared with the bond-based formulation would be at least twice as large (Sarego et al. 2016; Jafarzadeh et al. 2024). Given that the variability in material properties of glass, for example, is often higher than 5%, and the fact that we are concerned here with understanding the evolution of the damage and failure phenomenon in a brittle target, in this study we select the bond-based model.

The entire body is discretized into nodes, each with a known volume in the reference configuration. For simplicity, we use a uniform discretization. The failure patterns are not symmetric because the impact location is selected off-center, close to the impact location estimated from the experiments. This location may fall not at a node, but between discretization nodes, depending on the discretization.

To perform the spatial integration of the PD equations, we use the partial-volume integration algorithm (see details in Sect. 3 and Hu et al. 2010). The two plates (see Fig. 2) are at rest and in contact, but we do not enforce any constraints to mimic the tape applied in the experiment on the sides to keep the plates together. Therefore, after impact, in the computational model, our plates will eventually separate from one another. Nevertheless, as seen from Sect. 4.1, most of the damage takes place within the first 100 μs after impact, and the major differences between the presence or absence of the side tape are the following: with the tape, the PC plate's rebound is likely to cause some extra damage onto the glass plate, as well as reduced cracking on the edges of the sample because of stress waves being transmitted to the PC plate from the glass plate.

The damage index at a node is defined as the ratio between the number of broken bonds and the original number of bonds at that node. By plotting this index at all nodes, we can observe the evolution of cracks or diffuse-damage zones. When nodes with about 50% damage follow a clearly defined line or surface, that is an indication of the presence of a crack line or crack surface. Notice that in PD, when such damage happens, actual material separation takes place. This is in contrast with, for example, phase-field models (Borden et al. 2012; Aranson et al. 2000; Bourdin et al. 2008, 2011).

A convergence study in terms of the damage patterns created by the impact event can be performed by reducing the horizon size δ while keeping the ratio $m = \frac{\delta}{\Delta x}$, where Δx is the grid spacing, constant. This type of convergence is called δ-convergence (see Bobaru et al. 2009; Chen and Bobaru 2015) and, with the mid-point type spatial integration used here, the PD solution converges to the classical one for problems with no discontinuities. When damage is part of the problem, the grid factor m needs to be sufficiently large to allow for the existence of a sufficiently large number of bonds in all possible directions at a node, which will lead to unrestricted/grid-independent crack growth. For isotropic materials the m value of 4 or larger is recommended (see Ha and Bobaru 2011a) while for anisotropic materials a value of at least 5 is needed (see Dipasquale et al. 2016; Hu et al. 2012). Larger m values are always better for reducing the grid-dependence but they come with an increase in computational cost, and a balance has to be achieved between accuracy and cost. Larger values of m do not penalize efficiency in some recent fast algorithms for PD models (see Jafarzadeh et al. 2024, 2022).

The maps of damage in the glass plate for this convergence study are shown in Figs. 5, 21, and 44, for $\delta = 0.9$, 2, and 4 mm, respectively. We notice that the main failure modes are correctly captured[3] even when the horizon size ($\delta = 4$ mm) is larger than the 3.3 mm thickness of the plate. As the horizon size decreases, the damage patterns get refined, and we observe that the locations and extent of damage obtained by the peridynamic model approach those seen in the experiment (see Fig. 1). Previous results on convergence for dynamic brittle cracks in glass have indicated that a horizon size of around 1 mm is sufficiently small to predict the measured crack propagation speed (Ha and Bobaru 2011b). For more on convergence of PD models please see (Bobaru and Zhang 2015; Bobaru and Hu 2012).

The small differences between the results with a horizon size of 2 mm and 0.9045 mm (see Fig. 21 and

[3] In the sense explained in the beginning of Sect. 4.

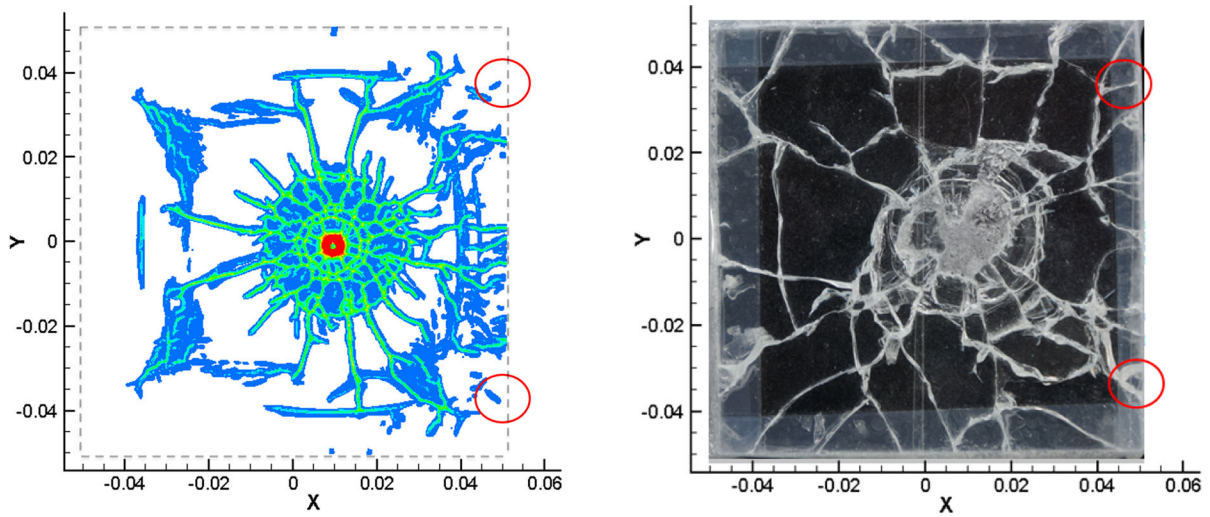

Fig. 43 Left: Damage map at 19.9 μs after impact, blanking all nodes with damage index less than 0.1; the edge-to-center cracks closest to the right corners of the plate are in the red circles; Right: The edge-to-center cracks identified in the experiment

Fig. 44 Damage maps for $\delta = 4$ mm at 99 μs from the time of impact. Strike face (left), back face (right), and cross-section through the impact point (bottom)

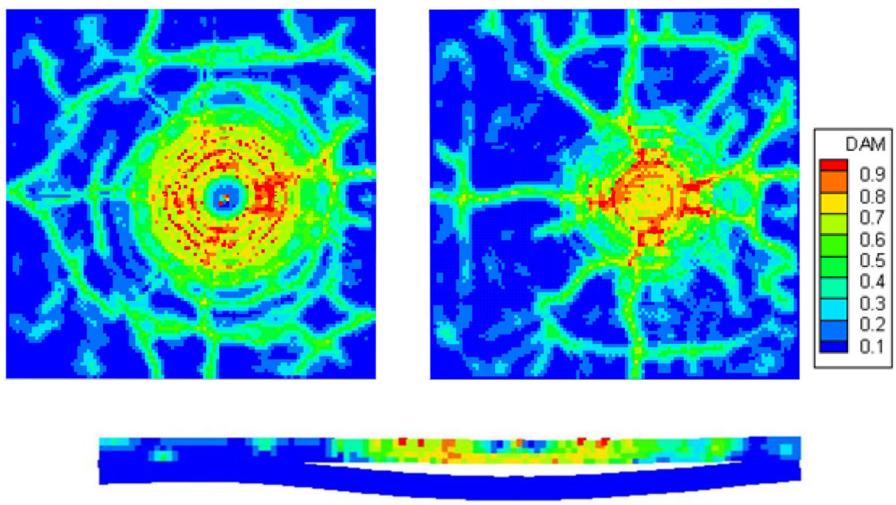

Fig. 5, respectively) confirm the conclusion that at these impact speeds, a horizon size of about 1 mm provides a converged result in the sense of the crack paths and types of damage observed.

References

Achenbach J (1973) Wave propagation in elastic solids. North-holland Publishing Company, Amsterdam

Aguiar AR (2016) On the Determination of a Peridynamic Constant in a Linear Constitutive Model. J Elast 122(1):27–39

Aguiar AR, Fosdick R (2014) A constitutive model for a linearly elastic peridynamic body. Math Mech Solids 19(5):502–523

Aranson I, Kalatsky V, Vinokur V (2000) Continuum field description of crack propagation. Phys Rev Lett 85(1):118

ASTM C1322-15 (2019), Standard Practice for Fractography and Characterization of Fracture Origins in Advanced Ceramics, West Conshohocken, PA: ASTM International.

Bless S, Chen T (2010) Impact damage in layered glass. Int J Fract 162(1–2):151–158

Bobaru F, Ha Y, Hu W (2012) Damage progression from impact in layered glass modeled with peridynamics. Open Engineering 2(4):551–561

Bobaru F, Hu W (2012) The meaning, selection, and use of the peridynamic horizon and its relation to crack branching in brittle materials. Int J Fract 176(2):215–222

Bobaru F, Xu Z, Wang Y (2016) Peridynamic Modeling of Impact and Fragmentation, in *Handbook of Peridynamic Modeling*, Taylor and Francis, pp. 381–407.

Bobaru F, Yang M, Alves LF, Silling SA (2009) Convergence, adaptive refinement, and scaling in 1D peridynamics. Int J Numer Meth Eng 77(6):852–877

Bobaru F, Zhang G (2015) Why do cracks branch? A peridynamic investigation of dynamic brittle fracture. Int J Fract 196(1):59–98

Borden MJ, Verhoosel CV, Scott MA, Hughes TJ, Landis CM (2012) A phase-field description of dynamic brittle fracture. Comput Methods Appl Mech Eng 217:77–95

Bourdin B, Christopher JL, Casey LR (2011) A time-discrete model for dynamic fracture based on crack regularization. Int J Fract 168(2):133–143

Bourdin B, Francfort G, Marigo JJ (2008) The variational approach to fracture. J Elast 91(1–3):5–148

Bowden FP, Field JE (1964) The brittle fracture of solids by liquid impact, by solid impact, and by shock. Proc R Soc Lond A 282(1390):331–352

Chaudhri MM (2015) Dynamic fracture of inorganic glasses by hard spherical and conical projectiles. Philos Trans A 373(2038):20140135

Chaudhri MM, Chen L (1986) The catastrophic failure of thermally tempered glass caused by small-particle impact. Nature 320:48–50

Chen Z, Bakenhus D, Bobaru F (2016) A constructive peridynamic kernel for elasticity. Comput Methods Appl Mech Eng 311:356–373

Chen Z, Bobaru F (2015) Selecting the kernel in a peridynamic formulation: A study for transient heat diffusion. Comput Phys Commun 197:51–60

Chen X, Chan AH (2018) Modelling impact fracture and fragmentation of laminated glass using the combined finite-discrete element method. Int J Impact Eng 112:15–29

Dipasquale D, Sarego G, Zaccariotto M, Galvanetto U (2016) Dependence of crack paths on the orientation of regular 2D peridynamic grids. Eng Fract Mech 160:247–263

Field F (1988) Investigation of the impact performance of various glass and ceramic systems," United States Army, European Research Office of the U.S. Army, London, England

Field JE, Sun Q, Townsend D (1989) Ballistic impact of ceramics. Inst Phys Conf Ser 102:387–394

Ha Y, Bobaru F (2010) Studies of dynamic crack propagation and crack branching with peridynamics. Int J Fract 162(1–2):229–244

Ha Y, Bobaru F (2011a) Characteristics of dynamic brittle fracture captured with peridynamics. Eng Fract Mech 78(6):1156–1168

Ha Y D, and Bobaru F (2011b) Dynamic brittle fracture captured with Peridynamics," *In ASME 2011 International Mechanical Engineering Congress and Exposition,* pp. 437–442. American Society of Mechanical Engineers

Hertz H (1881) On the contact of elastic solids. J Reine Angew Math 110:156–171

Henke SF, Shanbhag S (2014) Mesh sensitivity in peridynamic simulations. Comput Phys Commun 185:181–193

Hirobe S, Sato Y, Takato Y, Oguni K (2023) Numerical analysis of glass edge chipping by impact loading. Int J Fract 243(1):31–45

Hu W, Ha Y, Bobaru F (2010) Numerical intergration in peridynamics. University of Nebraska-Lincoln, Department of Mechanical and Materials Engineering

Hu W, Ha Y, Bobaru F (2012) Peridynamic model for dynamic fracture in unidirectional fiber-reinforced composites. Comput Methods Appl Mech Eng 217:247–261

Hu W, Wang Y, Yu J, Yen C-F, Bobaru F (2013) Impact damage on a thin glass plate with a thin polycarbonate backing. Int J Impact Eng 62:152–165

Jafarzadeh S, Mousavi F, Larios A, Bobaru F (2022) A general and fast convolution-based method for peridynamics: Applications to elasticity and brittle fracture. Comput Methods Appl Mech Eng 392:114666

Jafarzadeh S, Mousavi F, Wang L, Bobaru F (2024) PeriFast/dynamics: A MATLAB code for explicit fast convolution-based peridynamic analysis of deformation and fracture. J Peridynam Nonlocal Model 6:33–61

Knight CG, Swain MV, Chaudhri MM (1977) Impact of small steel spheres on glass surfaces. J Mater Sci 12(8):1573–1586

Kocer C, Collins RE (1998) Angle of Hertzian cone cracks. J Am Ceram Soc 81(7):1736–1742

Le Q, Bobaru F (2018) Surface corrections for peridynamic models in elasticity and fracture. Comput Mech 61:499–518

Lei Z, Rougier E, Knight EE, Zang M, Munjiza A (2021) Impact fracture and fragmentation of glass via the 3D combined finite-discrete element method. Appl Sci 11(6):2484

Marder M (2015) Particle methods in the study of fracture. Int J Fract 196(1):169–188

Niazi S, Chen Z, Bobaru F (2021) Crack nucleation in brittle and quasi-brittle materials: A peridynamic analysis. Theoret Appl Fract Mech 112:102855

Pyttel T, Liebertz H, Cai J (2011) Failure criterion for laminated glass under impact loading and its application in finite element simulation. Int J Impact Eng 38(4):252–263

Quinn GD (2006) NIST Recommended Practice Guide: Fractography of Ceramics and Glasses, Special Publication (NIST SP) - 960–16, September 26.

Rahman M, Michelitsch T (2006) A note on the formula for the Rayleigh wave speed. Wave Motion 43(3):272–276

Ravi-Chandar K (2004) Dynamic fracture. Elsevier, Amsterdam

Rudshaug J, Hopperstad OS, Borvik T (2023) Capturing fracture initiation and crack propagation of car windshields. Eng Fract Mech 290:109461

Sarego G, Le QV, Bobaru F, Zaccariotto M, Galvanetto U (2016) Linearized state-based peridynamics for 2D problems. Int J Numer Meth Eng 108:1174–1197

Seagraves A, Radovitzky R (2015) Large-scale 3D modeling of projectile impact damage in brittle plates. J Mech Phys Solids 83:48–71

Seleson P (2014) Improved one-point quadrature algorithms for two-dimensional peridynamic models based on analytical calculations. Comput Methods Appl Mech Eng 282:184–217

Sherman D (2000) Impact failure mechanisms in alumina tiles on finite thickness support and the effect of confinement. Int J Impact Eng 24(3):313–328

Sherman D, Tamir B-S (1988) Quasi-static impact damage in confined ceramic tiles. Int J Impact Eng 21(4):245–265

Silling SA (2000) Reformulation of elasticity theory for discontinuities and long range force. J Mech Phys Solids 48(1):175–206
Silling S (2005) Fragmentation modeling with EMU. Sandia National Laboratories, Albuquerquez
Silling SA (2014) Origin and effect of nonlocality in a compiste. J Mech Mater Struct 9(2):245–258
Silling SA, Askari E (2005) A meshfree method based on the peridynamic model of solid mechanics. Comput Struct 83(17):1526–1535
Silling SA, Bobaru F (2005) Peridynamic modeling of membranes and fibers. Int J Non-Linear Mech 40(2):395–409
Silling SA, Epton M, Weckner O, Xu J, Askari E (2007) Peridynamic states and constitutive modeling. J Elast 88(2):151–184
Song J-H, Wang HW, Belytschko T (2008) A comparative study on finite element methods for dynamic fracture. Comput Mech 42(2):239–250
Timmel M, Kolling S, Osterrieder P, Du Bois P (2007) A finite element model for impact simulation with laminated glass. Int J Impact Eng 34(8):1465–1478
Walley SM (2014) An introduction to the properties of silica glass in ballistic applications. Strain 50(6):470–500
Wang L, Mehrmashhadi J, Bobaru F (2023) Interfaces in dynamic brittle fracture of PMMA: a peridynamic analysis. Int J Fract 244:217–245
Xu Z, Zhang G, Chen Z, Bobaru F (2018) Elastic vortices and thermally-driven cracks in brittle materials with peridynamics. Int J Fract 209(1):203–222
Zhang G, Gazonas GA, Bobaru F (2018) Supershear damage propagation and sub-Rayleigh crack growth from edge-on impact: A peridynamic analysis. Int J Impact Eng 113:73–87
Zhang T, Li X, Gao H (2015) Fracture of graphene: a review. Int J Fract 196(1–2):1–31